POLITECNICO DI TORINO

Department of Environmental, Land and Infrastructure Engineering

Master's Degree in Environmental and Land Engineering
Specialization in Climate Change

Passive seismic monitoring of climate-driven rock slope instability: the Gollone landslide (Acceglio, CN, Italy)

Supervisor:

Chiara Colombero

Co-supervisor:

Lorena Di Toro

Student:

Francesca Ghigo – s346233

Academic Year 2025-2026

Acknowledgement

At the end of this journey, I would like to thank all the professors and colleagues I met along the way for creating a professional, friendly, and welcoming environment. The multicultural atmosphere I experienced has been one of the most enriching aspects of this journey.

A special thank you to my supervisor, Chiara Colombero, for giving me the opportunity to work on this project and for welcoming me into the team, and to Lorena Di Toro for her constant support, professionalism, and guidance.

I would like to thank all the people who have supported me every day, believed in me, and made these years happy and peaceful.

Most of all, I want to thank my family for giving me the opportunity to study, for their constant support, encouragement, and trust throughout these years.

Abstract

Landslides represent an important natural hazard in mountainous areas, and their evolution can be influenced by meteorological conditions.

Passive seismic monitoring has proven to be an effective tool to investigate internal changes within unstable rock masses through the variations of the resonance frequencies and ambient vibration characteristics.

This work aims to investigate the influence of meteorological forcing on the dynamic behaviour of the Gollone landslide (Acceglio, CN, Italy) by integrating passive seismic data, recorded by two monitoring stations, with meteorological observations, extensometer measurements, and numerical modelling. The analysis was structured according to data availability, instrumentation, and seismic data collection periods.

Seismic data were analysed through Power Spectral Density (PSD) and Horizontal to Vertical Spectral Ratio (HVSR) techniques, complemented by the azimuth analysis and a preliminary assessment of microseismic activity through the STA/LTA method.

Results highlight a strong influence of meteorological conditions on fracture dynamics. Historical landslide events were preceded by intense precipitation episodes and occurred during periods characterized by low, but generally positive temperatures. Extensometer data reveal that fracture opening accelerations are mainly related to snowmelt cycles, while precipitation appears to play a secondary role except during particularly intense rainfall events.

Seismic analyses identified two main resonance frequencies, approximately around 4-5 Hz and 6-8 Hz. HVSR amplitudes exhibited clear daily variations correlated with temperature fluctuations and cross-correlation analysis revealed an out-of-phase response of about 14 hours.

At longer timescale, meteorological cycles appear to modify the fracture constraints, causing variations in azimuth angle of vibration and changes in the relative contribution of the observed vibration modes.

Microseismic activity provided additional insights into the dynamic behaviour of the unstable rock mass.

The numerical model reproduced the first two observed resonance frequencies and supported the interpretation of the dominant vibration modes.

Overall, the results demonstrate the close relation between climate-driven processes and rock slope instability, providing valuable insights for long-term monitoring strategies and contributing to the development of early warning systems in the context of the ongoing climate change.

Table of Contents

List of Figures

List of Tables

Introduction

Rock mass instabilities represent a critical hazard that need to be characterize and monitor to prevent potentially dangerous impacts on urbanized areas or natural environments. In this context, geomatic techniques and in situ methods have always been used to track the evolution of slope deformations and macroscopic structural changes, however these approaches are still not effective in early warning, being that they cannot detect early internal modifications (Hausler et al., 2019; Burjanek et al., 2018; Colombero et al., 2021)

Within this framework, geophysics surveys, in particular passive seismic monitoring, add an important tool for prevention purposes. Passive seismic, in fact, can detect microscopic reversible or irreversible modifications in the stability of the mass through the identification of resonance frequencies (Colombero et al., 2021; Hausler et al., 2019).

Irreversible modifications correspond to processes that lead to permanent decrease in the rigidity of the rock mass. These are mainly associated to mechanical causes. Reversible modifications, instead, usually exhibit a cycle and are mainly driven by weather conditions, such as temperature, precipitation and snow accumulation. These reversible processes can temporally alter the mechanical and elastic properties of the material and restore after. Although long term repeated cycles can lead to a permanent modification of the properties (Colombero et al., 2021).

Therefore, in this work, particular attention is given to the application of passive seismic monitoring techniques for the investigation of the stability of the investigated landslide and on the influence of climate change on fracture dynamics.

Passive seismic

The passive seismic investigation techniques rely on the detection of naturally occurring seismic signals, without the deliberate generation of artificial seismic waves induced by the operator as it happens in active seismic investigation methods. The signals detected may originate from natural sources such as earthquakes, icequakes, fractures and sliding material, or from anthropogenic activities.

Both natural and anthropogenic phenomena produce ambient seismic noise. It consists of continuous and low amplitude vibration of the Earth generated by wind, weather systems, traffic, industrial activities and other sources, which usually are considered unwanted in seismic signal analysis, because they can mask or interfere with the seismic signals generated by the studied phenomenon.

Passive seismic methods can be applied at local or global scales both for site characterization and site monitoring.

The main phenomenon investigated is resonance. This effect is related to the contrast in acoustic impedance between different materials. In the field of gravitational instabilities, the resonance frequency can be approximated with a simple oscillator, following the relation:

$$f = \frac{1}{2\pi}\sqrt{\frac{K}{M}} \tag{1}$$

The resonance frequency is therefore directly proportional to the square root of the stiffness (K) and an inversely proportional to the square root of the mass of the system (M) (Colombero et al., 2018, Colombero et al., 2021).

This simple relationship highlights that a decrease in stiffness, associated with progressive damage and weakening of the rock mass, results in a drop of the resonance frequency values ("Dynamic response of the Chamousset rock column (Western Alps, France)", C. Lévy, L. Baillet, D. Jongmans, P. Mourot, and D. Hantz, 2010). Monitoring the resonance frequencies provide, therefore, a powerful tool for early warning.

The resonance frequencies are identified from peaks in the Power Spectral Density of continuous noise recordings. In addition, methods such as Horizontal to Vertical Spectral Ratio (HVSR), can be adopted to enhance these spectral peaks by filtering out the components of the ambient noise.

Response of rock fractures to climate change

Several studies, including Lévy et al. (2010), Burjanek et al. (2018), Colombero et al. (2018) and Bottelin et al. (2024), have investigated the relationship between meteorological conditions and landslide stability, focusing on fracture evolution and variations in resonance frequencies.

The key climatic variables affecting slope stability are temperature, precipitation and snow accumulation. Given that "warming of the climate system is unequivocal" (IPCC, 2014, p.40) is essential to consider how these climatic factors evolver under climate change.

Gariano et al. (2016) reviewed a large number of studies on the relationship between landslides and climate, noting that most of them report a causal relationship between landslides occurrence and climate change.

However, the current literature presents several limitations. First, studies are distributed unevenly and there are difficulties due to the different geographical and temporal scale at which climate processes and landslides operate. Moreover, most of the studies based the landslide-climate modelling analysis on single landslide case study.

In this context, Gariano et al. (2016) focused on collecting existing studies to assess the impacts of climate change on landslide activity at a regional to global scales.

Their preliminary results are shown in Figure 1.

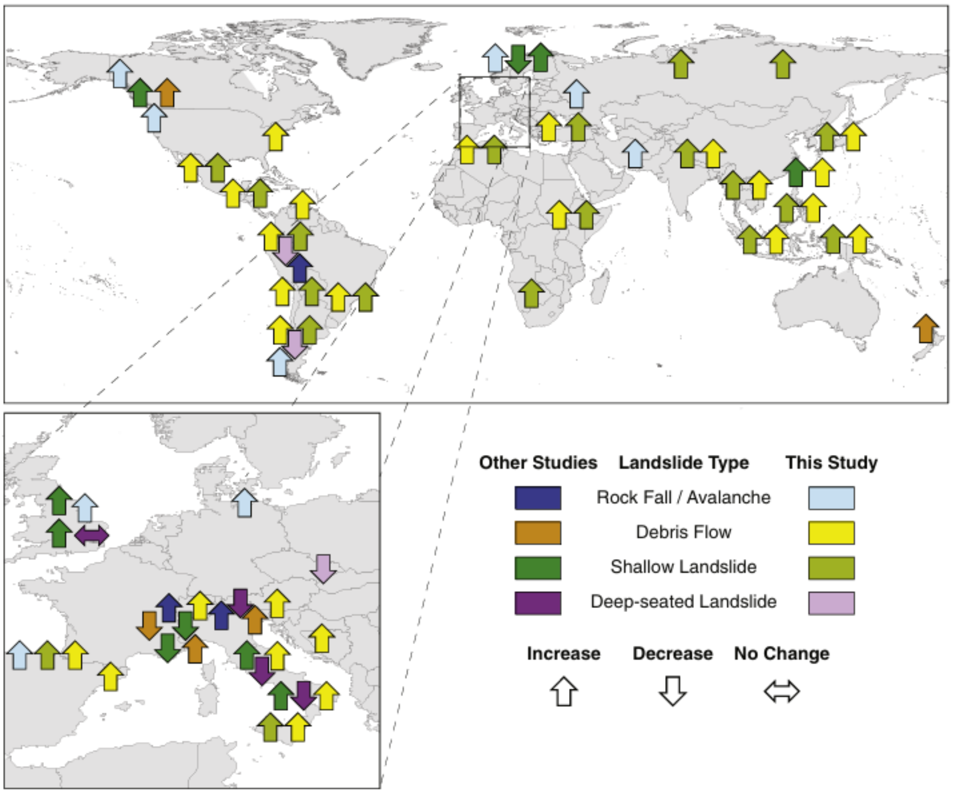

Figure 1: Map shows general areas of expected variations in the abundance or activity of four landslide types, driven by the projected climate change. Dark colours are projections from the literature and light colours are projections from this study. From "Landslides in changing climate", Gariano et al., 2020.

Determining whether landslide risk will increase or decrease in the future, and whether such changes are direct or indirect consequence of climate variations, remains challenging and requires further investigation.

Nevertheless, analysing how the different climatic factors influence landslide processes is a crucial step to improve future hazard and risk assessments.

The main processes affecting fractures, thus slope stability, are the thermo-mechanical and hydro-mechanical ones.

The following sections are primarily based on the results of Lévy et al. (2010), Bottelin et al. (2013) and Colombero et al. (2021).

Temperature driven mechanisms

The expansion and contraction of rock mass, due to temperature variations induce changes in fracture aperture (Colombero et al., 2021). When fracture openings decrease due to an increase in temperature, stiffness increases, leading to higher resonance frequencies (1) and seismic velocity variations (dV/V). The seismic wave velocity is given by;

$$V = \sqrt{\frac{G}{\rho}} \tag{2}$$

Where G is the shear rigidity of the material and ρ is its density.

Due to (2), an increase in the rigidity of the material may result in a reduced risk of rock detachment (mass M).

Conversely, when temperature decreases, the fractures open, reducing stiffness and leading to lower resonance frequencies and lower dV/V values.

Bottelin at al. (2013) observed resonance frequency variations are in phase with the air temperature variations at daily scale, with a delay of few hours (observed also by Lévy et al. (2010)). While at seasonal scale show a delay of approximately three months. However, a significant difference in the response time to temperature variation is observed between sites (Colombero et al., 2021).

Temperature variations can also modify stress conditions within the rock mass due to the different thermal dilation between the surface and the internal portion of the rock. Differential expansion can generate internal stresses that increase the bulk stiffness of the rock mass, therefore, as seen before, increase in resonance frequency and dV/V.

In addition, temperature can also affect the intrinsic elastic properties of the rock mass, in particular an increased temperature leads to a decrease in Young’s modulus (E) (Brotons et al. (2013)).

In fact, as temperature increases, atomic vibrations become larger, reducing the stiffness of interatomic bonds. Consequently, less stress is required to produce a given strain, leading to a decrease in the Young's modulus (Mirnezhad et al., 2012).

Precipitation driven mechanisms

Water seepage resulting from intense rainfall or snowmelt can increase the groundwater level and pore water pressure within the slope. This, leads to an increase in the destabilizing forces acting on the unstable mass, typically followed by the decrease in resonance frequency.

In the meantime, the increase in water content raises the bulk density of the material, reducing its rigidity and resulting in a decrease of seismic velocity variation dV/V in accordance with equation (2).

During freezing periods, water within fractures can freeze and form ice. Ice formation temporally increases contact stiffness, with consequent increase in resonance frequency (up to 300% in some areas). The increase in resonance frequency may persist also for several months (Colombero et al., 2021).

However, repeated freeze-thaw cycles can damage rock bridges reducing the resonance frequency (Lévy et al. (2010)).

Aim and objectives of the study

The aim of this work is the characterization of the dynamic behaviour of the Gollone landslide (Upper Maira Valley, Western Alps, Italy) by integrating passive seismic monitoring, extensometer measurements, meteorological observations and numerical modelling. Moreover, this study aims to investigate the mechanisms controlling fracture evolution and rock-slope stability, with particular focus on how meteorological conditions affect the unstable rock mass, in order to explore the implications for landslide hazard assessment and early warning.

The study is divided into four main chapters, following the chronological development of the available monitoring network.

The first chapter covers the period from 2010 to 2021 and investigates the two landslide events occurred in 2011 and 2019 using meteorological data.

The second chapter, from 2021, integrate the meteorological analysis with the extensometer measurements.

Finally, the third and fourth chapters further expand the analysis by incorporating data from the geophones installed by Politecnico di Torino in 2024. These two chapters are treated separately because they are based on two different data collections.

Site characterization

The Gollone landslide is located in the Piedmont region (north-west of Italy) within the municipality of Acceglio (CN). The landslide lies on the north-eastern slope of the Monte Midia Soprano in the upper Maira Valley.

The geographical location of the study area is illustrated in Figure 2(a), which shows the position of the site at different spatial scales.

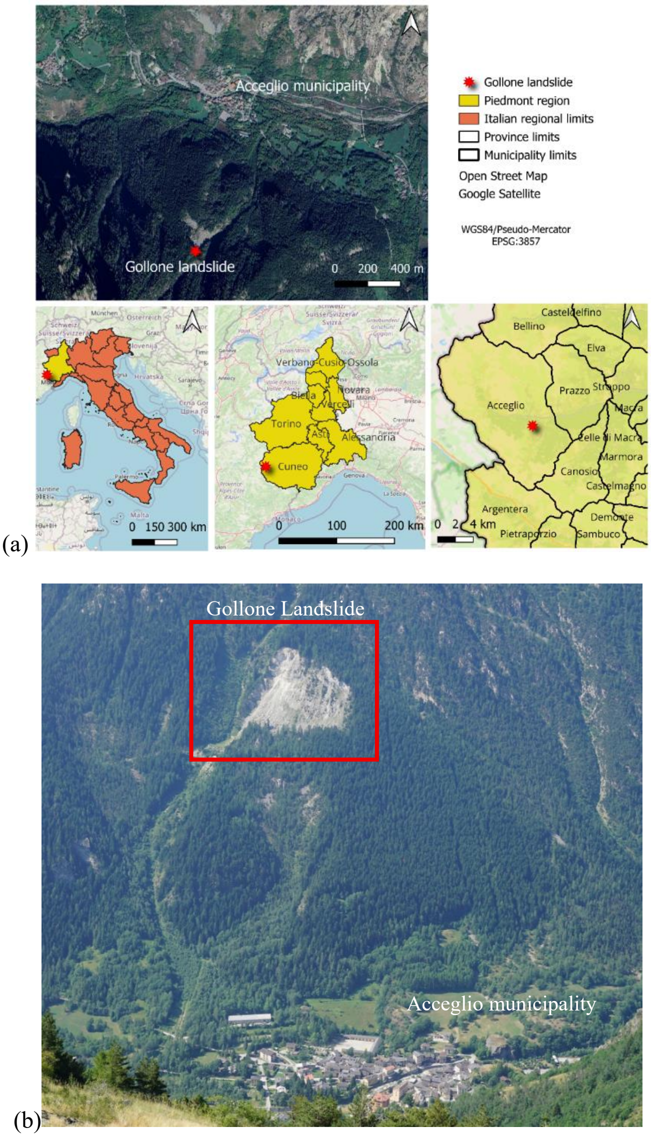

Figure 2: (a) Site location of the Gollone landslide. Maps drawn in QGIS. (b) Overview of the landslide slope taken from the opposite slope, picture taken the 25th July 2019 and linked to SiFraP report 2024.

Petroccia et al. (2020) investigated the structural and geomorphological framework of the entire upper Maira Valley, with an excursus on the Gollone landslide.

The study area is characterized by two different lithological units, the Acceglio Unit and the Upper Piedmont Zone, Figure 3 (a). The first consists of metavolcanic rocks, quartzite and marble, the second one of calcschists with lenses of serpentinite and metabasite.

The quartzite-marble contact crops out in the southwestern part of the upper Maira Valley, within the Gollone landslide. The erodibility of these materials significantly influences the landslide mechanisms and the triggering conditions also if the two have different behaviours and produces different impacts in terms of movement styles and velocities.

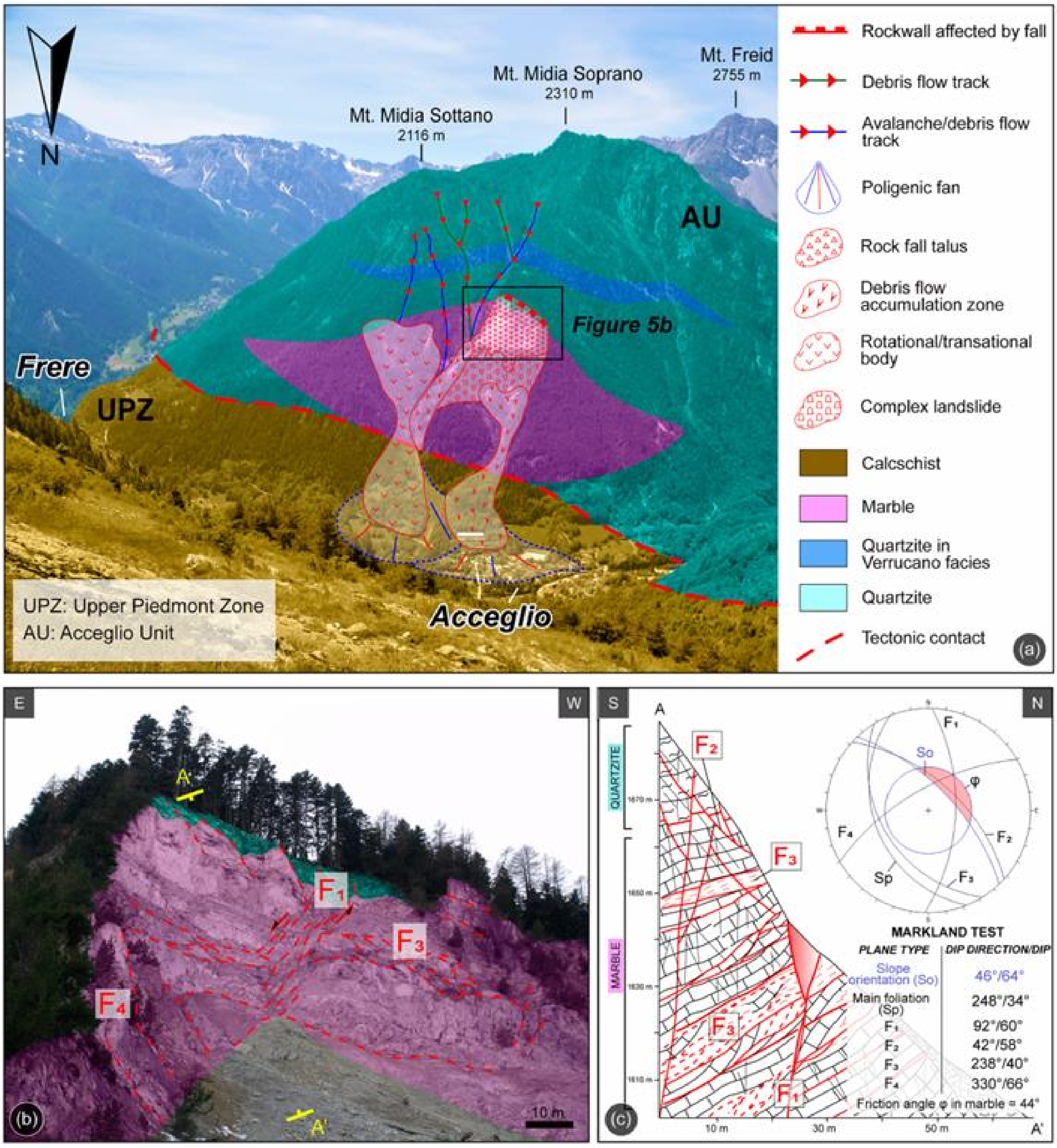

Figure 3: (a) Main geomorphological elements and lithotypes in the Gollone landslide area. (b) Mesostructural view from the base of the Gollone landslide. (c) Structural-geological schematic cross-section and Markland test reported. From "Structural and geomorphological framework of the upper Maira Valley (Western Alps, Italy): the case study of the Gollone Landslide", A. Petroccia et al., 2020.

The landslide crown, oriented NW–SE, is located at an elevation of approximately 1700 m, whereas the valley lies at about 1220 m, resulting in an overall elevation difference of 480 m. The detachment zone is characterized by a sub-vertical scarp approximately 250 m long and about 70 m high, being the main source area of the instability.

As seen in Figure 3 (a), the main movements typologies are rockslide, slow movements of accumulation, rock falls and debris flows.

The most dangerous elements in this area are, therefore, the unstable detrital cover and the unstable rock masses from the detachment zone.

Four main fractures have been detected in this area through the Markland test by Petroccia et al. 2020, among them the one investigated by this work is located in the upper part of the landslide, right below the lithological contact between marble and quartzite (Figure 3 (b, c)).

Background and landslide history

In September 2024, the SIFraP – Sistema Informatico Fenomeni Franosi in Piemonte (Codice frana: 004-60692-00 and Codice frana: 004-00678-00) classified the Gollone landslide in its summary sheet as a fall/topple type, characterized by extremely rapid velocities (>5 m/s) and a dormant state of activity.

Several landslide events have been documented in this area over the years. The earliest recorded occurrences date back to the late 18th century and the early 19th, while a major event in 1846 was probably caused by intense precipitation (A. Petroccia et al. (2020)).

More recently, an avalanche event in 2008-2009 contributed to the removal of high vegetation that characterizes the area today (A. Petroccia et al. (2020)).

A photograph of the interested sector from 2008 is shown in Figure 4.

Figure 4: Gollone landslide at the 25 June 2008. From ARPA Piemonte, SIFraP report, 2013

The first reactivation event occurred between 4 and 6 December 2011, more precisely at 10:45 a.m. on 4 December and at 4:00 p.m. on 6 December.

According to SIFraP, the total failed volume was around 20000 m^3. A close inspection of the scarp and the landslide crown revealed the presence of unstable rock masses isolated by fractures with centimetric apertures. The widest fracture reaches almost one meter and delimits a huge rock with an estimated volume of around 15000 m^3.

It is also important to note that Regione Piemonte, on 21 November 2011 published a report about the intense hydro-meteorological event that occurred between 4 and 8 November 2011. Although Acceglio was not among the main involved municipalities, this event may still be considered relevant, as the nearby municipality of Canosio was significantly impacted (Figure 5). The situation after the landslide of December 2011 is shown in Figure 6.

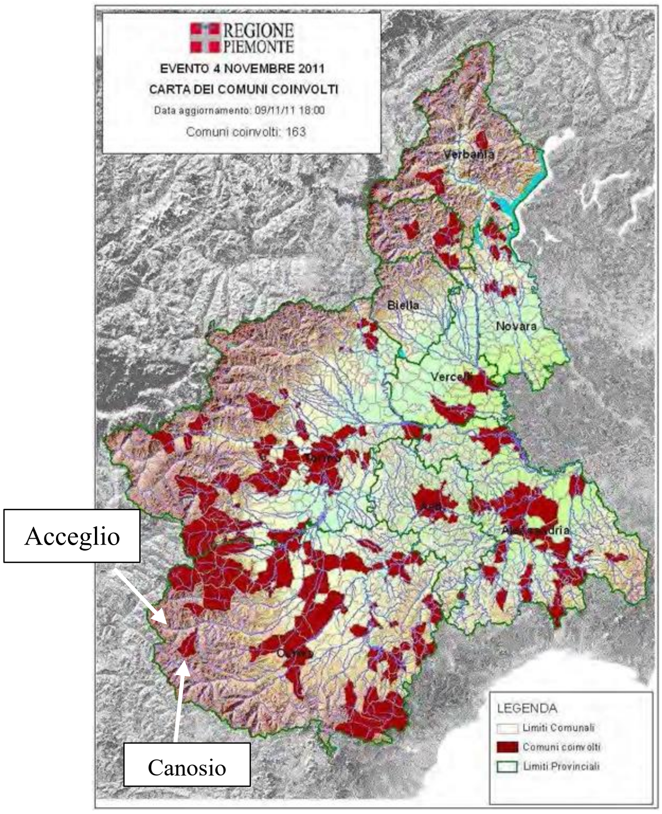

Figure 5: Main involved municipalities in the hydro-meteorological event of the 4 November 2011. From the Regione Piemonte's report about the hydro-meteorological event of the 4-8 November 2011.

Figure 6: Gollone landslide at the 29 May 2012. From ARPA Piemonte, SIFraP report, 2013

Figure 7: Zoom on the Gollone landslide at the 29 may 2012. From ARPA Piemonte, SIFraP report, 2013

The two rock sections highlighted in Figure 7 correspond to two unstable rock masses, both characterised by fractures at their upper portions. The one on the right is associated with the fracture monitored and investigated in this work, where an extensometer was installed for monitoring purposes by ARPA Piemonte. The rock mass on the left detached during the landslide event occurred in the night between the 28 and 29 October 2019 (Figure 8).

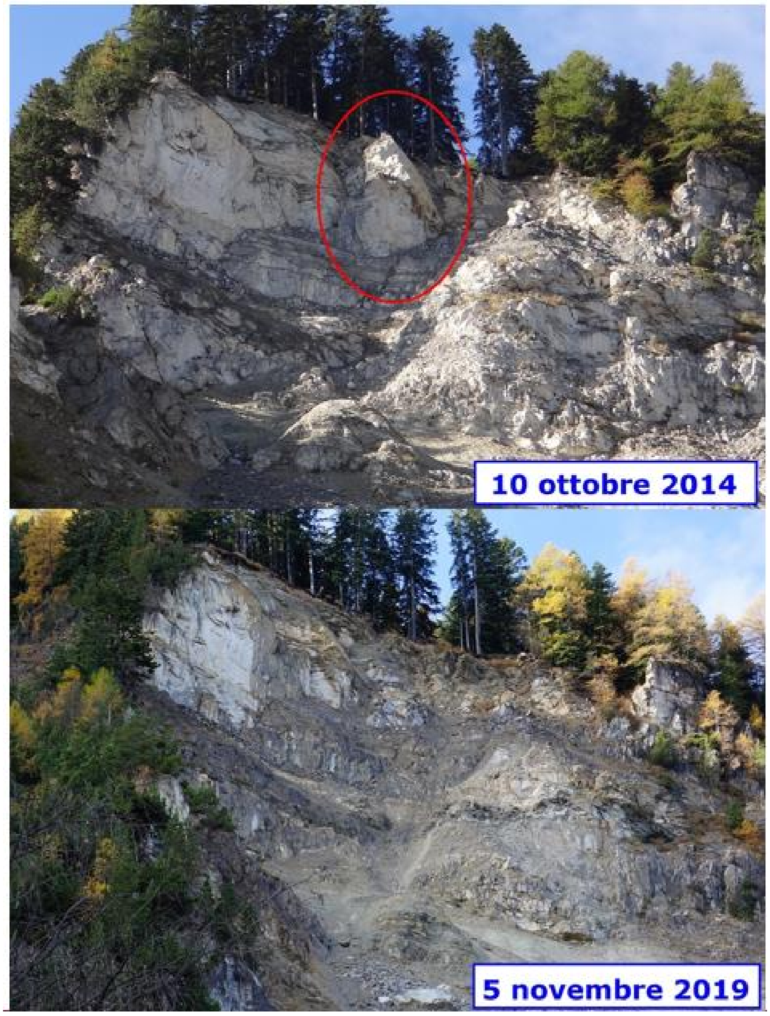

Figure 8: Gollone landslide difference before and after the 2019's detachment. From "Geosciences IR – Gollone (Acceglio)", C. A. Stefanini, G. M. Marmoni, Sapienza di Roma, 2024.

Protection systems

As reported in the report published by SiFraP, ARPA Piemonte in 2013, following the detachment occurred in 2011 some interventions took place to reduce the risk.

In the upper section of the Gollone landslide an artificial barrier, that consist in two rock fall protection embankments and an intermediate catchment area, was constructed with local material. This protection system provides a storage capacity of around 10000 m^3 (Figure 9(b)).

The upstream embankment is 4 m high and 35 m long, while the downstream one is 7 m high and 45 m long.

In the downstream part of the Gollone landslide two earth embankments were constructed in November 2012. Those are positioned longitudinally to the slope and have the purpose to protect some isolated buildings from potential boulders that could travel down the channel located on the eastern side of the Gollone landslide. Totally these embankments are 65 m large and 2.5 m high.

Earlier in the '90s, an embankment consisting of a rock armour base topped with reinforced soil (120m long and 5m high) was realized to protect the municipality of Acceglio from the avalanches that from the Monte Midia can detach and run down in the channel. Later on the opera was enlarged, adding a 3m high and 60m long embankment to the previous one.

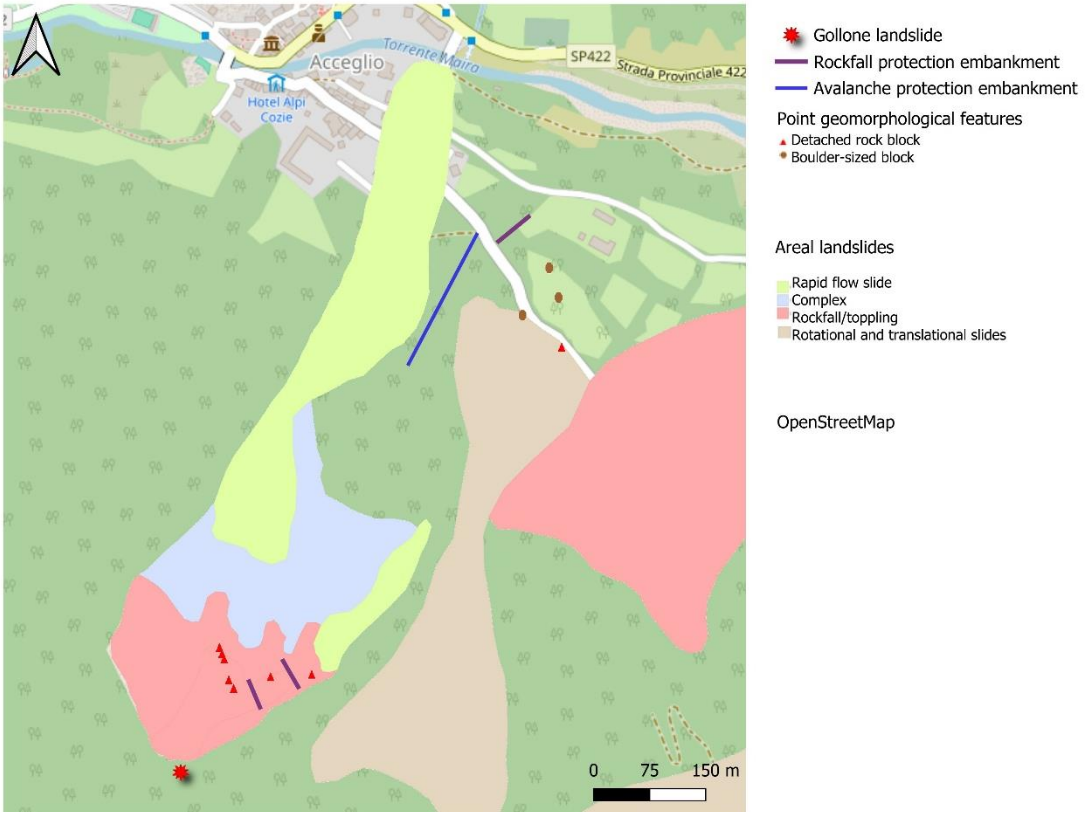

(a)


(b)

Figure 9: (a) Protection systems map, map produced in QGIS (b) Embankment realised after the landslide of 2011, picture taken the 29 December 2011 and linked to SiFraP report 2024.

Monitoring network

The monitoring tools included a topographic system for surface displacements measurements, based on an automated theodolite installed at the Acceglio cemetery (

Figure 10). This system operated from November 2010 to October 2012 and then form September 2015 to October 2017.

From October 2019 to November 2020 the extensometer installed across the fracture highlighted a cumulative opening of 12 mm. The instrument was later replaced, and in November 2021 ARPA Piemonte installed a new wire extensometer (Figure 11) to continue monitoring the fracture on which the large unstable rock block is still resting.

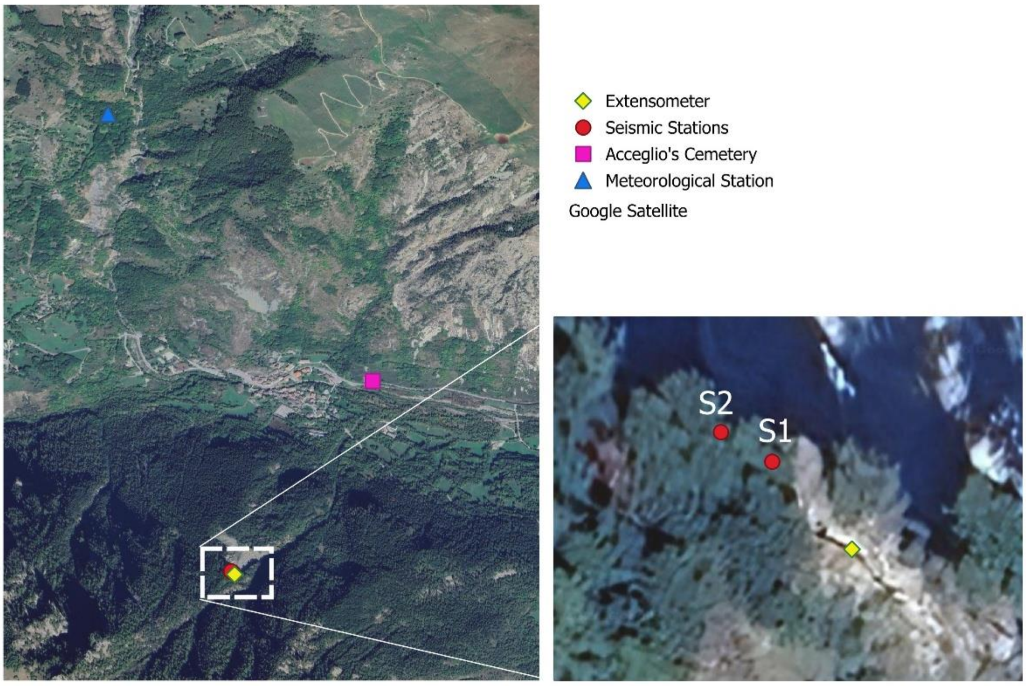

Figure 10: Monitoring network positions. Map obtained in QGIS.

Figure 11: Wire extensometer installed by ARPA Piemonte in 2021. Image taken on the 28 May 2024.

The data recorded by the extensometer are shown in Figure 12.

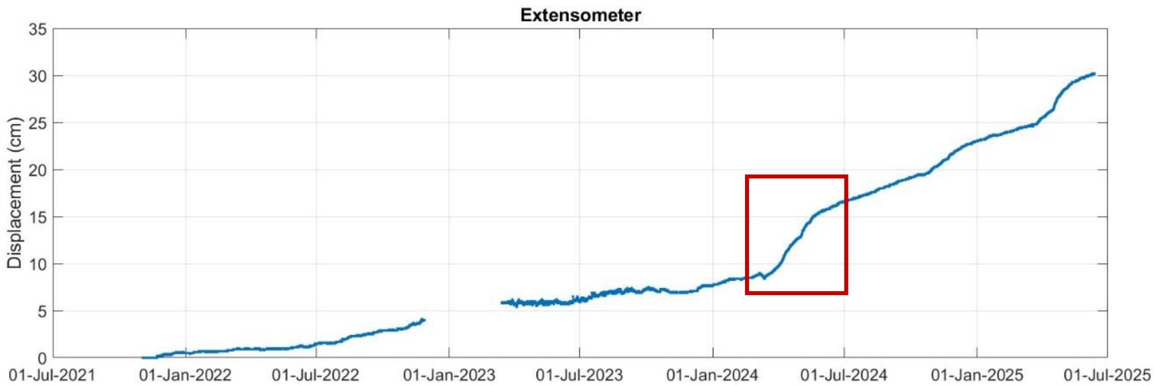

Figure 12: Evolution of the extensometer displacement since the installation.

An important acceleration in the displacement was observed around April 2024. This event led to the installation, on the 28 May 2024, of seismic monitoring network by the DIATI department of the Politecnico di Torino in order to better monitor the evolution of the landslide.

Station S2 was positioned on the stable sector as a local reference while the S1 was installed on the unstable volume (Figure 13).

Figure 13: Location of the two geophones. Image taken on the 28 May 2024.

Each station consists of a three-component seismometers (Trillium Compact Horizon, 20 s, Nanometrics), a data acquisition and storage system (Pegasus, Nanometrics), and a power supply system composed of a battery and a solar panel.

Each station continuously records with a sampling frequency of 250 Hz on the two horizontal components (E and N) and the vertical component (Z).

Station S1, located within the unstable area (Lon: 6.988016; Lat: 44.466186), continuously recorded until early September 2024, after which the data acquisition becomes intermittent. Station S2 (Lon: 6.987954; Lat: 44.466223) recorded continuously until the 15 September 2024.

The monitoring network was complemented by the meteorological data, including hourly and daily records of temperature, precipitation and snow cover, obtained from the ARPA Piemonte database at the Acceglio Colombata meteorological station (UTM X = 339567 m, UTM Y = 4927939 m, elevation = 1590 m;

Figure 10), and were used to support the analysis of this study.

Methods

Ambient seismic noise spectral analysis

As previously discussed, the concept of resonance in gravitational instabilities can be interpreted in analogy with a simple oscillator, characterized by a fundamental resonance frequency f1 controlled by the ration between system stiffness and unstable mass. According to equation (1), the resonance frequency increases with increasing stiffness and decreases with the unstable mass.

This resonance frequency can be identified through the spectral analysis of ambient seismic noise, by detecting peaks in the Power Spectral Density (PSD) of continuous ambient noise recordings.

To enhance these spectral peaks and better characterize site response, spectral ratio techniques can also be applied, including single-station approaches like Horizontal-to-Vertical Spectral Ratio (HVSR) method. In this study both PSD and HVSR analysis have been employed to investigate the resonance frequencies of the unstable slope.

Prior to the computation of both PSD and HVSR, the continuous noise recordings were pre-processed to ensure the stability and reliability of the results (Colombero et al., 2018).

First, each signal was demeaned and detrended to remove constant and linear components that could bias the low-frequency content.

To limit the influence of transient and high energy events, a data clipping procedure was applied using an adaptive threshold set to four times the standard deviation of the entire detrended and demeaned signal.

Each 1-hr recording was than divided into shorter, non-overlapping windows of 100 s duration. Each segment was tapered using a 10% cosine function in order to reduce spectral leakage associated with finite windowing, improving the stability and smoothness of the Fast Fourier Transform (FFT).

This segmentation strategy allowed a reduction in the variance of the spectral estimates by increasing the number of independent realizations.

The same pre-processing workflow adopted for PSD computation was consistently applied prior to spectral ratio computation, ensuring methodological coherence between the different analyses.

Finally, the Fourier transform was applied to each of the three components (Vertical, North, and East), producing the spectra used in subsequent analyses.

Power Spectral Density (PSD)

The Power Spectral Density was computed to quantify the frequency dependent distribution of the seismic noise energy, providing a fundamental tool for evaluating the spectral content of ambient vibrations.

Different studies over the years have analysed the seismic background noise statistically, defining models to provide reference benchmarks for seismic data interpretation. These benchmarks have been used to assess the data quality.

In particular, the Peterson curves, known as the New Low Noise Model (NLNM) and New High Noise Model (NHNM) define the typical range of background seismic noise (J. Peterson, 1993). These models are derived from data collected in 75 seismic stations worldwide, analysing for each frequency the maximum and the minimum power registered.

Figure 14 shows the overlap of the maximum and minimum power spectral densities recorded at different stations.

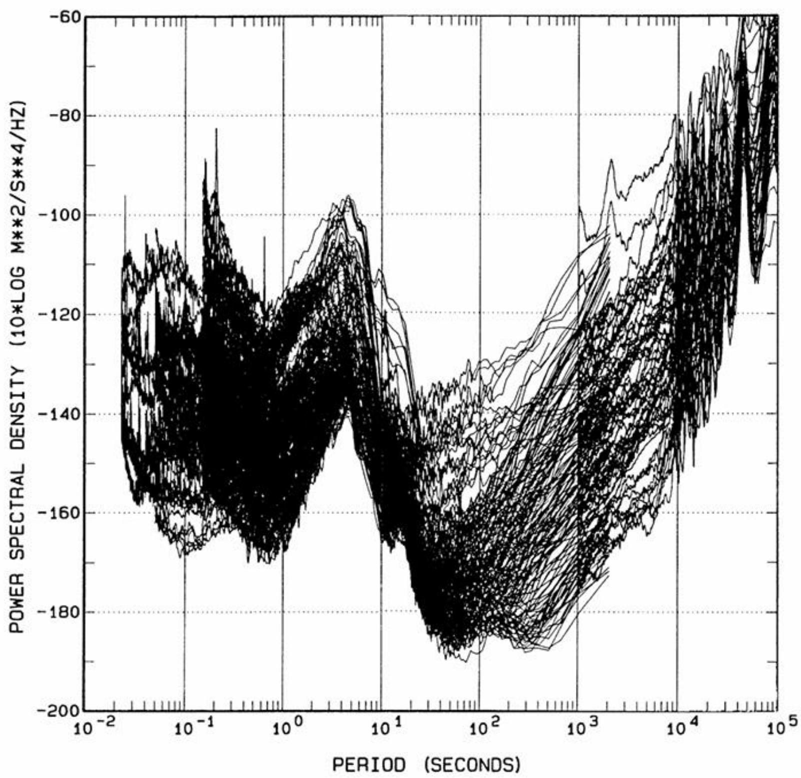

Figure 14: Overlay of station spectra. Form "Observations and modelling of seismic background noise", J. Peterson, 1993, p.14

The new noise model was defined graphically fitting straight line segments to the lower and upper envelopes of the spectral overlay.

The result of the fit of the new noise model, together with the fit of the original noise model (Brune and Oliver, 1959) are reported in Figure 15.

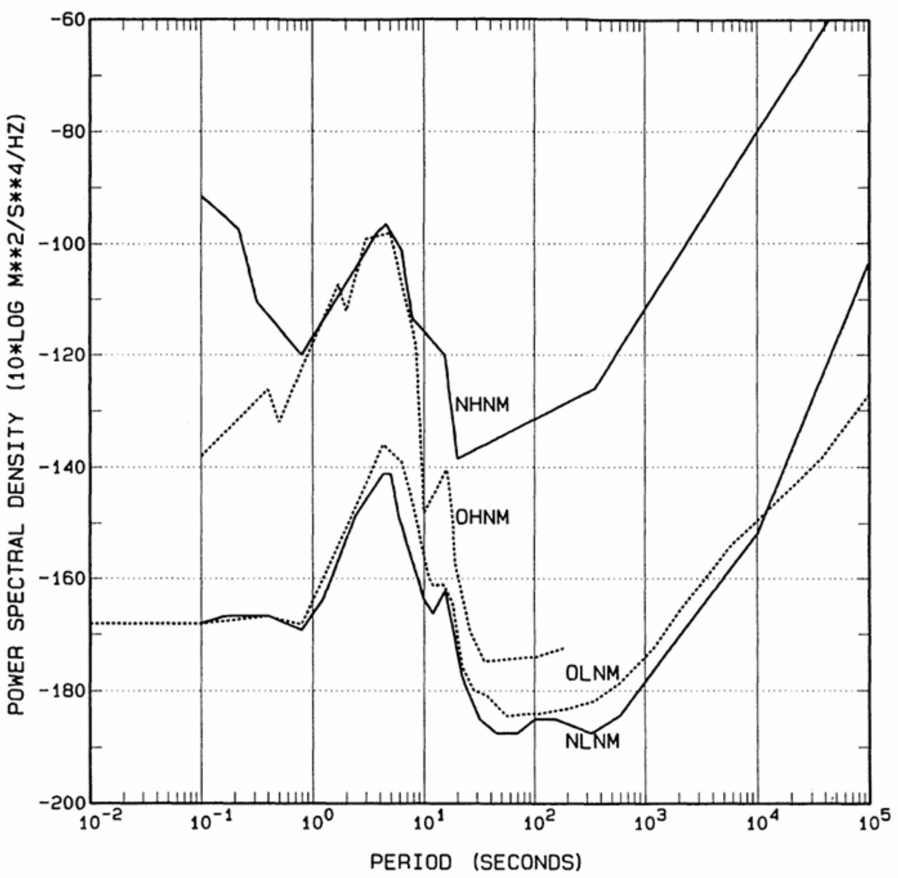

Figure 15: Comparison of the new (NLNM, NHNM) and the original noise models (OLNM, OHNM). Form "Observations and modelling of seismic background noise", J. Peterson, 1993, p.35

Signal close to the NLNM indicate quiet sites, with minimum noise level, good for detecting weak seismic events, whereas signals near the NHNM represents the maximum noise level, often related to human activity or strong environmental conditions.

Therefore, to evaluate the performance of seismic stations is important to compare the recorded spectra with the Peterson curves.

While the PSD provides a quantitative measure of the spectral energy content of the recorded noise, this information alone may not be sufficient to identify reliably the site-specific resonance frequencies. To complement the PSD analysis and enhance the detection of resonance peaks, the Horizontal to Vertical (H/V) spectral ratio method was therefore applied, as it emphasizes frequency dependent amplification by comparing the horizontal and vertical components of ground motion.

Horizontal to vertical spectral ratio (H/V)

To further investigate the site response and identify resonance frequencies, the Horizontal to Vertical Spectral Ratio (H/V or HVSR) technique was applied. It is a non-invasive passive method that relies on measurements at a single station.

HVSR curve can be classified based on its shape. In particular, well-defined peaks generally indicate a strong subsurface velocity contrast, while HVSR peaks of low amplitude are related to weak contrast. Flat curves with little or no amplification are typically associated to rock sites. HVSR curve becomes more complex in the presence of irregular basement-sediments interfaces, faults or other topographic features (Maresca et al., 2022).

The H/V method is computed in the frequency domain as the ratio between the horizontal and vertical components of ground motion:

$$HVSR = \frac{H_f}{V_f} \tag{3}$$

Where H_f and V_f represent the horizontal and vertical spectral amplitudes, respectively.

The resulting horizontal spectrum (H_f) was obtained through the square root of the sum of the two orthogonal horizontal components (N and E) squared (Equation 4), while the vertical spectrum (V_f) was taken directly from the vertical channel.

$$H_f = \sqrt{N_f^2 + E_f^2} \tag{4}$$

Where N_f and E_f are the Fourier spectra of the north-south and east-west components, respectively.

The peaks observed in HVSR curves were interpreted as resonance frequencies, corresponding to frequencies at which ground motion is amplified.

In addition, the temporal evolution of the HVSR curves were analysed in order to assess possible time-dependent changes in resonance frequencies, peak amplitudes, and overall site-response characteristics.

Azimuth

To further characterize the site response, the azimuth of horizontal vibrations was computed from the North (N) and East (E) components of the recorded signals.

For each time window, the spectral amplitudes of the two horizontal components were combined to determine the predominant orientation of ground vibration in the horizontal plane.

The azimuth angle can be defined as:

$$\theta = arctan\left(\frac{E_f}{N_f}\right) \tag{5}$$

Where E_f and N_f represent the spectral amplitudes of the east and north components, respectively, and $\theta = 0°$ correspond to the north direction.

The azimuth provides information on the preferential direction of vibration, and can help identify directional trends associated with local structural features, and add directional information into the characterization of site response to PSD and H/V analysis.

The temporal evolution of the azimuth was also investigated to assess possible correlations with external factors such as meteorological variations. In fact, similarly to resonance frequencies and amplitude of the spectral peaks, the predominant vibration direction may vary over time in response to variation in weather conditions (Colombero et al., 2021)

Microseismicity

Microseismic monitoring is a passive seismic method used to identify microseismic events embedded in the ambient seismic noise. These events can be generated by different phenomena such as rock falls, crack propagation, meteorological forcing, or regional and local earthquakes. In this framework, microseismic analysis is generally used to detect, classify and locate short-duration events. The most interesting events we want to detect are those related to rock mass fracturing because their temporal trend can provide useful information about progressive damage and possible acceleration to failure.

To extract the microseismic events in the long-term continuous microseismic recording, the definition of a trigger algorithm becomes essential in the characterization of the seismic behaviour of a site.

The basic principle is that an event is detected when a the predefined threshold is exceeded.

Among the available techniques, the Short-Term Average over Long-Term Average (STA/LTA) algorithm is the simplest and wider used method in weak-motion seismology. Moreover, its application is particularly proper in seismically quiet sites where natural seismic noise represent the dominant source of background disturbance (Ltd, 2019).

The STA/LTA method continuously computes the ratio between two moving-time windows: a short-time window (STA) and a long-time window (LTA). When their ratio exceeds a predefined amplitude threshold, an event is detected and recorded.

The proper selection of the trigger parameters is fundamental for achieving reliable event detection. Trnkoczy (1999) discussed the main characteristics that should be considered in the definition of these parameters.

The short-time window represents an instantaneous measure of the seismic signal amplitude. Its duration must be longer than a few periods of a typical seismic signal but shorter than the shortest expected event. By adjusting the STA window it is possible to prioritize the capturing of distant or local event: shorter STA duration increases the trigger's sensitivity to short lasting local event, while longer STA windows reduce this sensitivity.

The long-time window provide an estimate of the average background seismic noise amplitude, and should, therefore, be significantly longer than the typical periods of noise fluctuations. By modifying it, the recording becomes more or less sensitive to regional events.

Ultimately, the STA/LTA trigger threshold determines which signals are classified as events and which are rejected. Higher threshold values reduce the number of detected events and limit the occurrence of false triggers, but may also result in the loss of weak but potentially relevant events. On the other hand, a too low threshold may generate a large number of false triggers. Therefore, the best STA/LTA threshold strongly depends on the seismic noise conditions of the monitored site.

The additional parameters set are:

Table 1: Parameters for the STA/LTA event detection method

Short time window	0.2 s
Long time window	10 s
STA/LTA trigger on	5
STA/LTA trigger off	1.5
Post-trig	5 s
Pre-trig	2 s

While the trigger threshold defines the STA/LTA ratio above which an event is detected, the detrigger threshold defines the ratio below which the event is considered concluded. The Pre-trig represent the amount of signal recoded before the threshold is reached, the Port-trig corresponds to the signal recorded after the detrigger threshold has been crossed. Both of them ensure that the recorded event is complete.

A schematic representation of the STA/LTA mechanism of selection is reported in Figure 16.

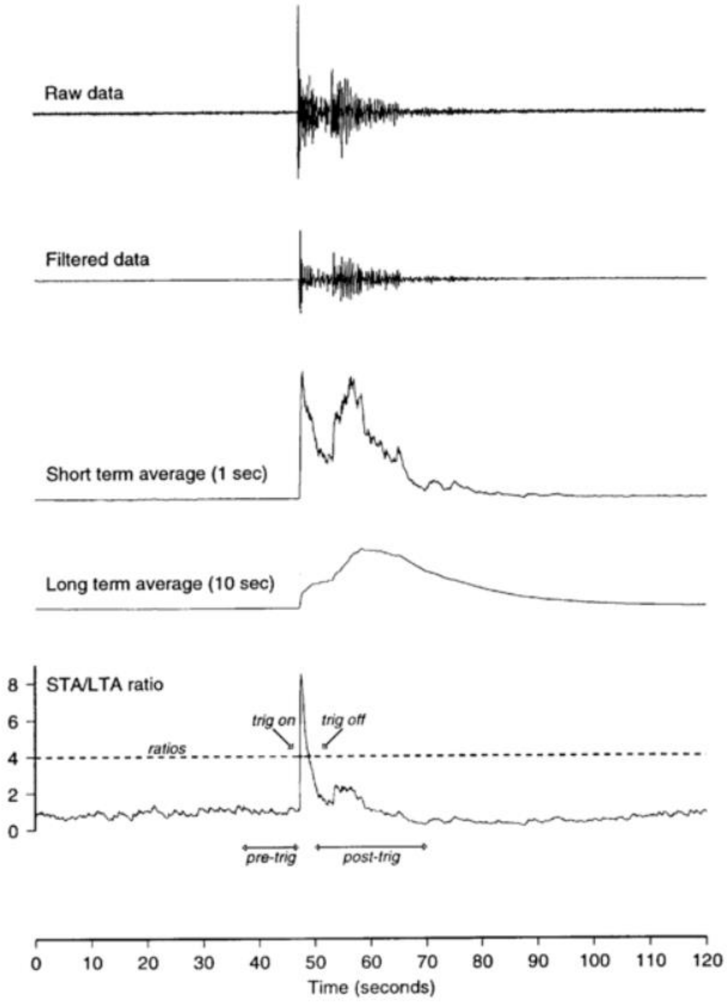

Figure 16: Illustration of the STA/LTA algorithm process (Ltd, 2019). From top to bottom: (1) incoming continuous seismic signal (raw data); (2) band-pass filtered signal; (3) short-term average (STA) of the absolute signal amplitude; (4) long-term average (LTA) of the absolute signal amplitude; (5) STA/LTA ratio used for event detection, showing the trigger-on and trigger-off thresholds, together with the pre-trig and post-trig recording windows..

Once events detection was concluded, a visual classification process was applied for station S1, for the events covering the period form 28 May 2024 to 22 August 2024. This process was based on events spectrograms, that is a graphical representation of the frequency spectrum of a signal over time (time and frequency domain), but also on the seismogram (amplitude of the seismic trace over time) and on the Fourier amplitude spectrum (amplitude of the signal versus frequency). Previous studies (e.g., Helmstetter et al. 2010; Levy et al. 2011) identified some classes, including:

- Rockfalls;
- Earthquakes;
- Microearthquakes;
- Microcracks.

Generally, large monitoring campaigns may generate thousands of recorded events, therefore manual classification becomes impractical. Consequently, machine-learning approaches are commonly employed to automatically cluster events according to their waveform similarity, allowing efficient identification of the main classes of seismic signals. However, in this study, all events were classified through visual inspection only.

Numerical model

Numerical modelling provides the opportunity to reproduce the geometry of the fracture and simulate its dynamic response under different conditions. In particular, it enable the identification and analyse of the system vibration modes, which are strongly influenced by fracture geometry and material properties. These parameters represent the main input of the model.

The simulation was carried out using COMSOL Multiphysics, a finite element analysis software.

The model was initially built by creating, combining and subtracting multiple block-shaped domains in order to reproduce the geometry of the fractured medium. Specific material properties, such as Young's modulus, density and Poisson's ratio, were than assigned to each domain.

Once the geometry and material properties were defined, COMSOL discretized the entire model into a finite element mesh. The governing equations of linear elasticity were then solved numerically over this mesh, allowing the software to compute the natural vibration modes of the system.

Results

All data processing and manipulations analysis presented in this work have been carried out using MATLAB software.

Meteorological analysis associated with historical landslide events (2011 and 2019)

As previously discussed, the two major landslide events affecting the Gollone area occurred between 4-6 December 2011 and 28-29 October 2019.

Given the well-established relationship between gravitational events and meteorological factors, temperature, precipitation, and snow accumulation data recorded at the meteorological station of Acceglio Colombata were analysed to investigate the possible triggering factors of these failures.

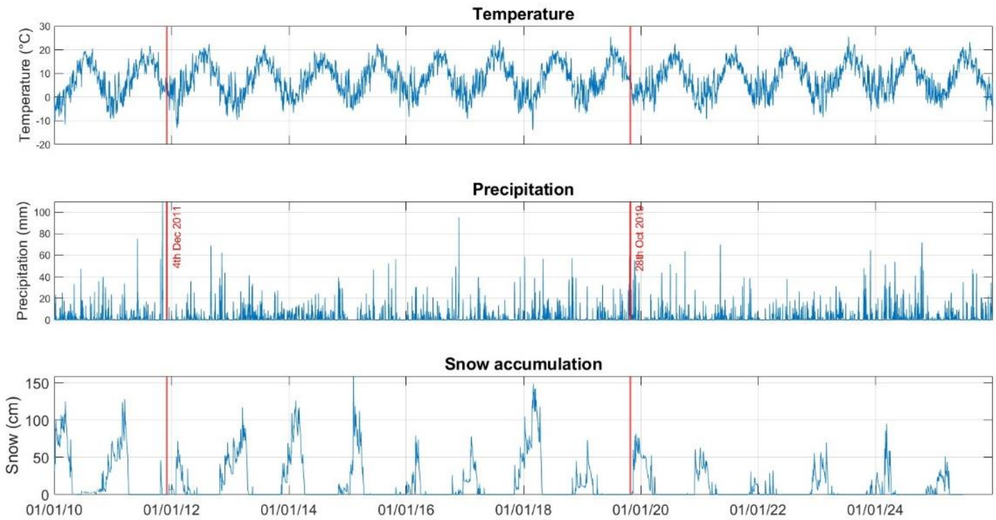

Figure 17: Mean daily temperature, precipitation and snow accumulation from 1st January 2010 to 31st December 2025 recorded at the Acceglio Colombata meteorological station. Red lines indicate onset of the two landslide events in 2011 and 2019. Data source: ARPA Piemonte.

Both landslide events occurred in the winter season, thus in low temperatures conditions. Although, the mean daily temperatures were lightly above 0 °C in both cases, and the failures were registered right before the onset of the main seasonal snow accumulation period (Figure 17).

As previously discussed, when temperatures decrease, the fracture may open, due to thermal contraction of the rock mass, resulting in a reduction of the overall stiffness. Nevertheless, during freezing periods (i.e., periods with temperature below 0 °C), the water that is present in the fractures may freeze and form ice. The presence of ice in fractures can temporarily increase contact stiffness between fracture surfaces.

With regard to temperature conditions, the occurrence of failures during periods characterized by low temperatures, but not by freezing conditions, is therefore consistent with findings reported in literature.

It is also important to note that both events occurred prior to the main phase of snow accumulation. During periods of significant snow accumulation, air temperatures are frequently below 0 °C, promoting freezing conditions within the fractures. In such conditions, snow cover may further contribute to the stabilization of the system, acting as a “binding” layer, while the freezing of water within the discontinuities leads to a temporary increase in contact stiffness, as previously discussed.

Moreover, the influence of snow cover on fracture aperture is limited during the accumulation phase. Its effect becomes more evident during the snowmelt periods, when increasing temperatures and water infiltration promote fracture opening.

To better visualize the meteorological conditions associated with failure occurrences, two detailed views of Figure 17 were produced, focusing on the years in which the failure occurred, 2011 and 2019.

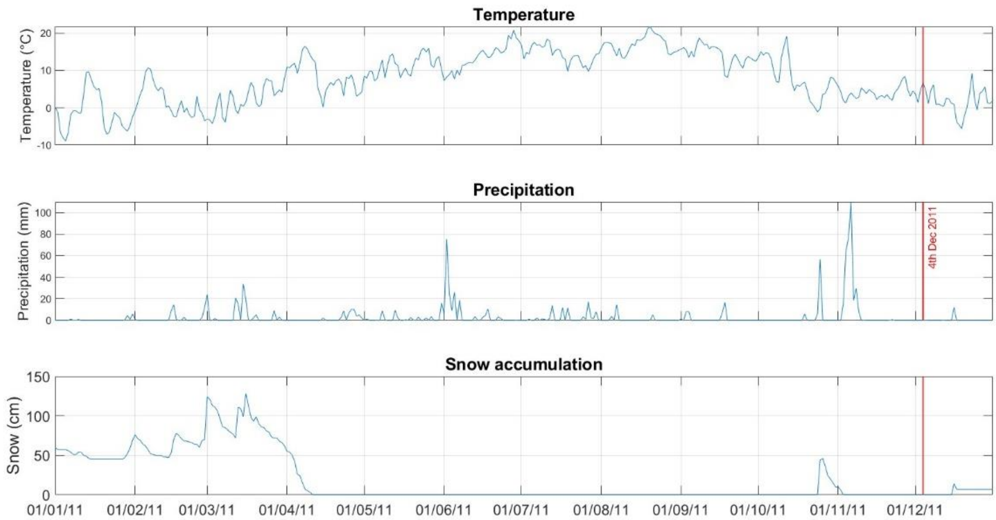

Figure 18: Detailed view of meteorological data recorded during 2011. The red line indicates the onset of the landslide event.

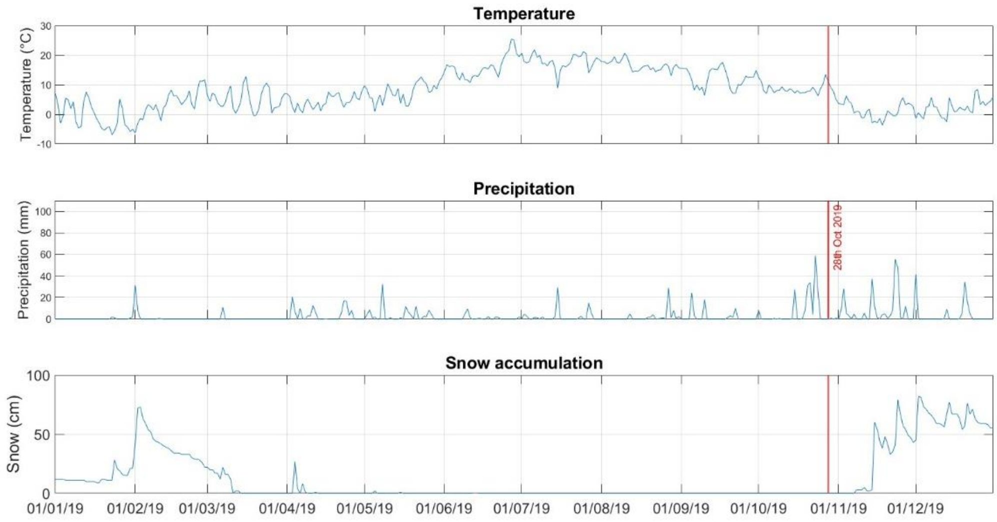

Figure 19: Detailed views of meteorological data recorded in 2019. The red line indicates the onset of the landslide event.

These zoomed-in plots suggests that snow accumulation was not a primary controlling factor for the observed events.

Both landslide events were preceded by significant precipitation episodes. In particular, a peak rainfall event of 58.5 mm occurred on the 23 October 2019, five days before the detachment. Similarly, an intense precipitation period was observed between 4 and 8 November 2011, as reported in the Regione Piemonte Report and shown in Figure 5. This represent the most intense event recorded over the 2010-2025 period, with a daily peak of 109.6 mm on 6 November 2011, approximately one month before the failure.

Meteorological data represent the only available information for the period prior to 2021, since neither the extensometer nor the seismic stations were installed at that time.

Despite these limitations, the meteorological analysis remains of primary importance, as it provides additional evidence supporting the role of meteorological factors as potential triggers of rock slope failures. In both events, the observed conditions are consistent with those commonly associated with failure in the literature, suggesting that precipitation and temperature may have contributed to the triggering of the collapses.

It is important to note, however, that such conditions do not necessarily lead to failure. Rather, they represent periods during which the probability of occurrence is increased compared to background conditions.

This contributes to a better understanding of the conditions that may favour future landslide occurrence and provides useful indications for identifying periods during which enhanced attention and monitoring are recommended.

Extensometer data and correlation with meteorological variables (2021–2025)

To better monitor the landslide an extensometer was installed from ARPA. The data used in this work are the one of the second device installed in November 2021.

The fracture's displacement graphs are reported in Figure 20. The first graph shows the absolute displacement over time, while to the second one has been applied a linear detrending, highlighting the deviations from the average linear trend of fracture opening.

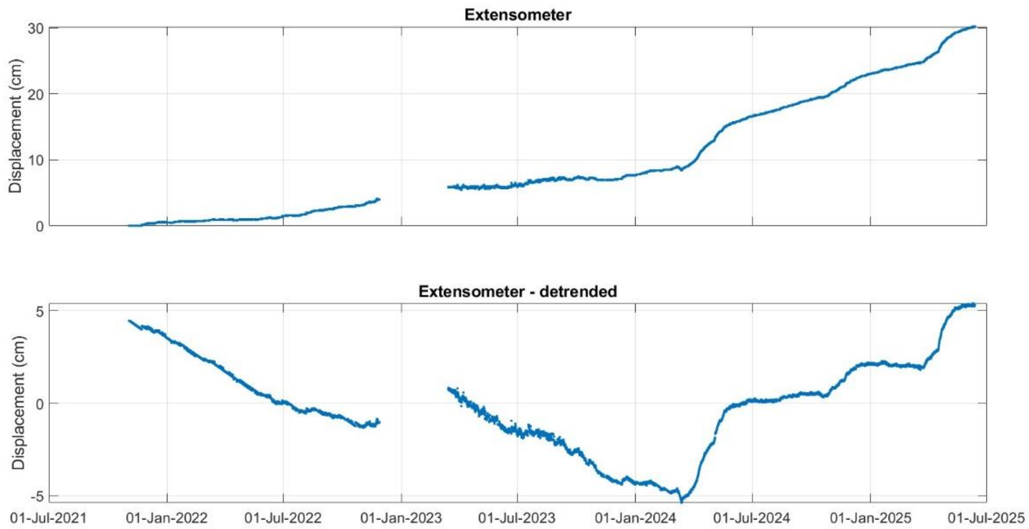

Figure 20: Displacement evolution in time recorded by the extensometer of ARPA Piemonte, between 2 November 2021 to 12 June 2025.

The data indicates a continuous opening of the fracture throughout the monitoring period, but the displacement rates vary over time, as shown in the second graph.

Significant accelerations in fracture opening can be used for early warning purposes, since this behaviour can precede rock detachments. Anyway, variations in displacement rate may not be only driven by mechanical factors but also by meteorological conditions. For this reason, the extensometer measurements were therefore compared with the main meteorological parameters.

As in the previous section, the purpose of this comparison is again to evaluate the influence of environmental conditions on fracture dynamics and to identify possible correlations between climatic forcing and variations in fracture opening. Within this framework, the extensometer data provide the additional opportunity to directly investigate the mechanical response of the monitored fracture.

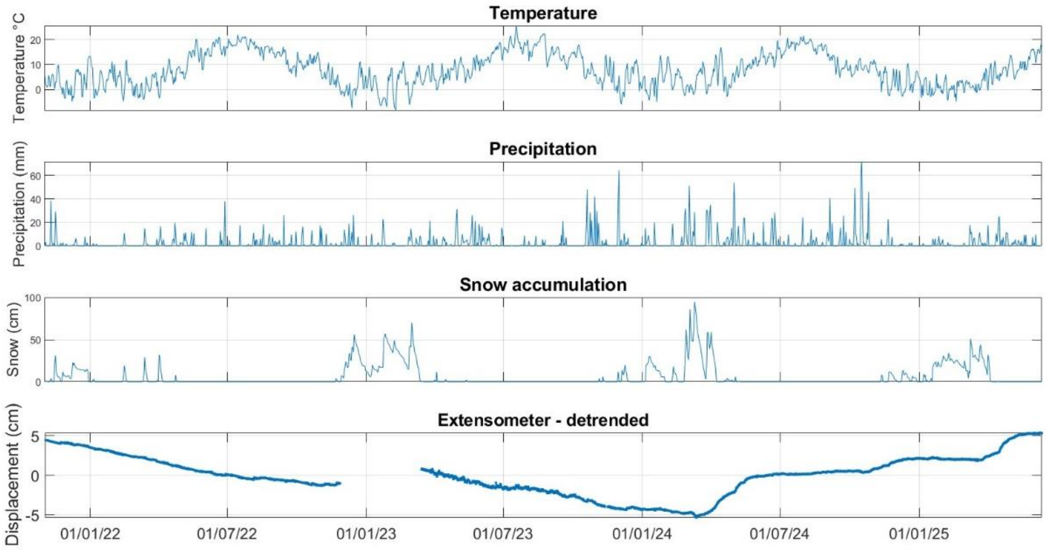

Figure 21: Mean daily temperature, precipitation and snow accumulation recorded at the ARPA Piemonte meteorological station of Acceglio, together with the detrended displacement measured by the ARPA Piemonte extensometer. Data span from 2 November 2021 to 12 June 2025.

This comparison suggests that the displacement of the fracture is not influenced by precipitation events, except for the most intense precipitation event occurred on the 17 October 2024 with 71.9 mm of rain. That event in fact was followed by a relative acceleration in fracture opening, as seen in Figure 22 b.

Most of the displacement acceleration events occurred during periods of low temperature, particularly in the final phase of freezing periods, when temperature is below 0 °C, or immediately afterward. As seen before the low temperature condition is commonly observed during the occurrence of these phenomena, anyway the main driving mechanism in this case can be attributed to the snow cycle.

Figure 22 a highlights a clear correspondence between periods of displacement acceleration and snow accumulation, with a slight time lag.

This behaviour is consistent with the hypothesis that the presence of snow or ice can temporarily increase the stiffness by acting as cement agent in the fracture. During the melting phase, when temperature rises above 0°C, this cementation effect disappears, while the fracture maintains the dilatation due to the volumetric expansion of water during freezing.

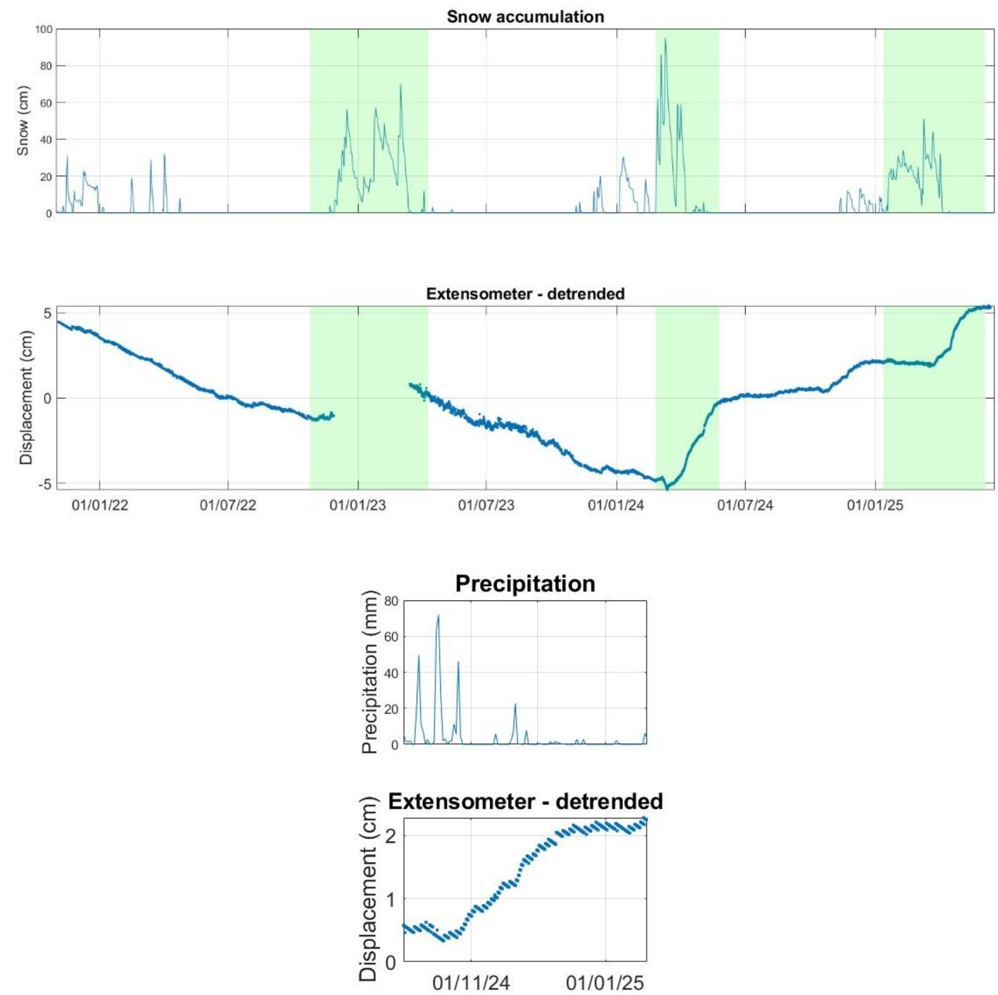

(a)

(b)

Figure 22: (a) Detailed view of the relationship between snow accumulation and fracture displacement acceleration. (b) Detailed view of the precipitation event of 17 October 2024 and its relationship with the displacement acceleration.

Seismic stations analysis results for the first data collection (28th May 2024 – 18th March 2025)

Power Spectral Density (PSD)

This section presents the Power Spectral Density (PSD) analysis of the data from the two seismic stations, with the aim of identifying the dominant frequency components of the ambient vibration signal.

The results reported in Figure 23 refer to the period between 28 May 2024 (date of seismic station installation) and the 15 September 2024, when station S2 stopped recording.

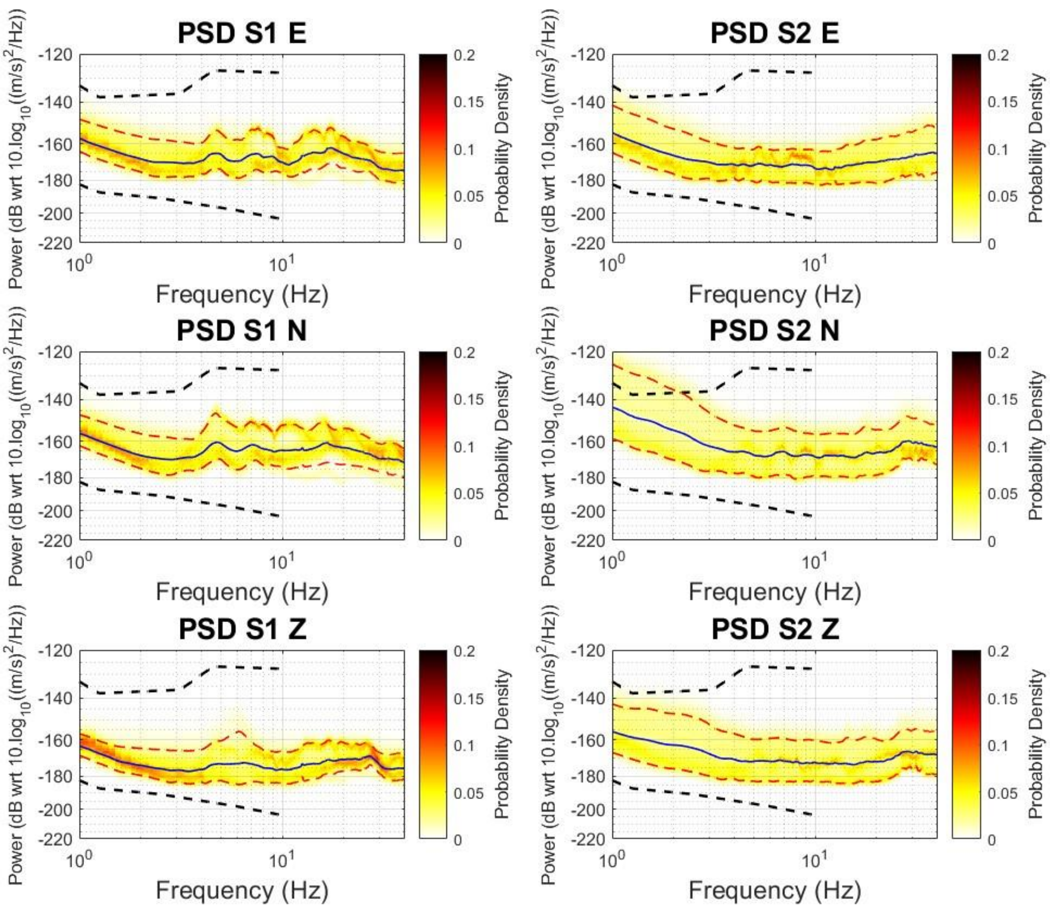

Figure 23: PSD probabilistic distribution for the two seismic stations in the three directions (E, N and Z) during the period between 28 May 2024 and 15 September 2024. Black dashed lines are the Peterson curves, blue line is the mean PSD and the red dashed lines correspond to the 10th and 90th percentiles.

The PSD distributions obtained from the station S2 are more stable in all the three components compared to PSDs of station S1, where some pronounced peaks are observed. This result is consistent with the different locations of the two geophones, with S1 installed on the unstable rock mass and S2 on the stable side of the fracture.

For station S1, the two horizontal directions exhibit a clear spectral peak between 4 and 5 Hz, that can be interpreted as the first resonance frequency of the unstable rock mass. A second peak is observed around 7 and 8 Hz, more evident in the Eastern component. In the vertical component, the main peak is at around 6 Hz.

The presence of peaks at different frequencies in the three components reflects different modes of vibration of the unstable rock mass.

Another difference can be observed considering that the colour scale is the probability density of PSD occurrences, highlighting the most recurrent spectral power levels. The S2 spectra shows a more uniform distribution of occurrence over a broader power range, indicating greater variability in the spectral amplitudes. On the contrary, S1 spectra shows a narrower PSD range between the 10^{th} and the 90^{th} percentiles and a higher concentration of occurrence around the median PSD values, especially at high and low frequencies. Within in the intermediate frequency band, where the resonance peaks are observed, the distribution of occurrence become more dispersed, suggesting increased variability in the spectral response.

Despite the different spectral variability observed between the two stations, the overall PSD power levels remain comparable for the analysed frequency. Considering the proximity of the stations, this suggests that both are exposed to similar ambient noise conditions and the observed differences are related to the distinct mechanical behaviour of the stable and unstable portions of the rock mass.

Regarding the Peterson curves, the PSD values of almost all the components fall within the range bounded by the New High Noise Model (NHNM) and the New Low Noise Model (NLNM), indicating that the recorded signals are consistent with typical environmental noise conditions.

The only exception is the N-S component of station S2, which exceeds the NHNM at low frequencies. Given the close proximity of the stations and the fact that this behaviour regards only one component, the behaviour cannot be related to a large-scale environmental noise.

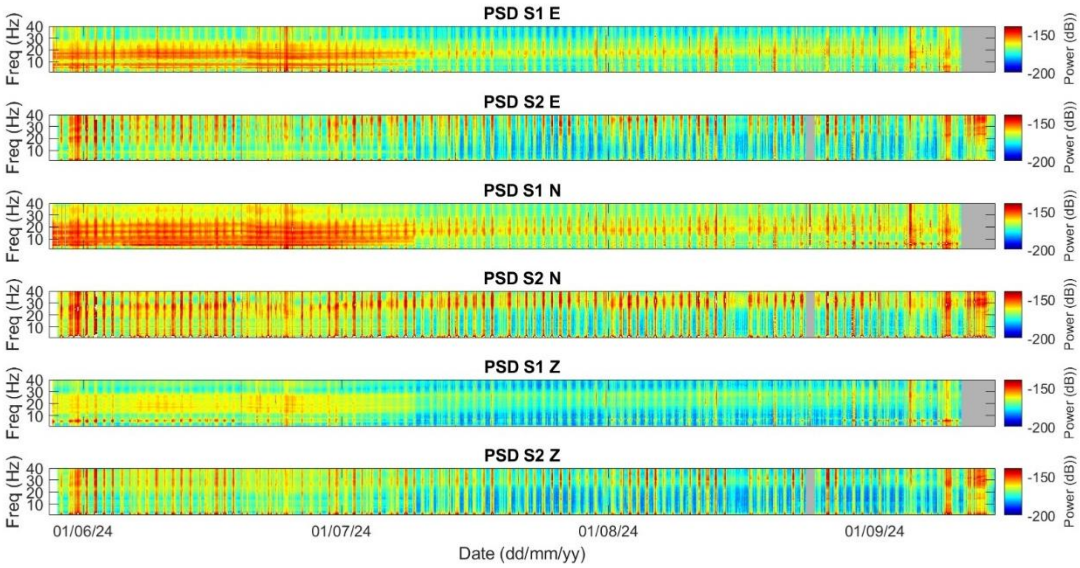

Figure 24: Temporal evolution of PSD for the two seismic stations in the three components during the period between 28 May 2024 and 15 September 2024. PSD values are expressed in decibels (dB), computed as $10log10(PSD)$, where the reference value is 1 (m/s)²/Hz. Grey areas indicate periods with missing data.

To further investigate the temporal variability of the seismic signals, the evolution of the PSD over time was analysed for each station and component (Figure 24). While the probabilistic distributions provide an overall statistical characterization of the spectral content, the time-dependent PSD analysis allows the identification of transient variations and persistent frequency bands throughout the recording period.

It is evident that, the PSD amplitude of the signal drastically change after 9 July 2024, especially for the station S1. This behaviour is more clear in the H/V results (Figure 25) and will therefore be discussed in the following chapter.

Moreover, PSD amplitude appear to follow a daily cycle and the trend seems similar with the typical daily temperature cycle, suggesting a possible influence of thermal forcing on the seismic response.

Horizontal to vertical spectral ratio (H/V)

Following the analysis of the Power Spectral Density (PSD) of the signals, the Horizontal-to-Vertical Spectral ratio (H/V) was investigated to further characterize the spectral response of the monitored rock mass.

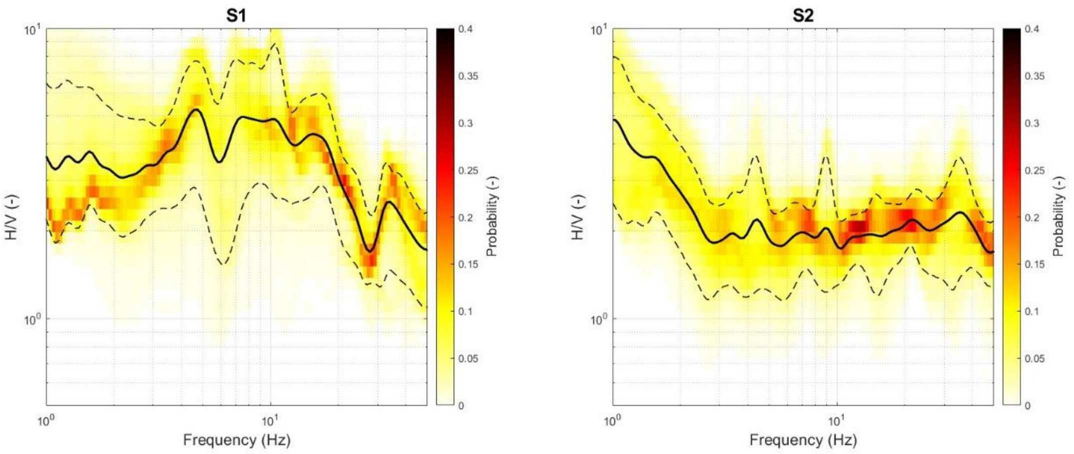

(a)

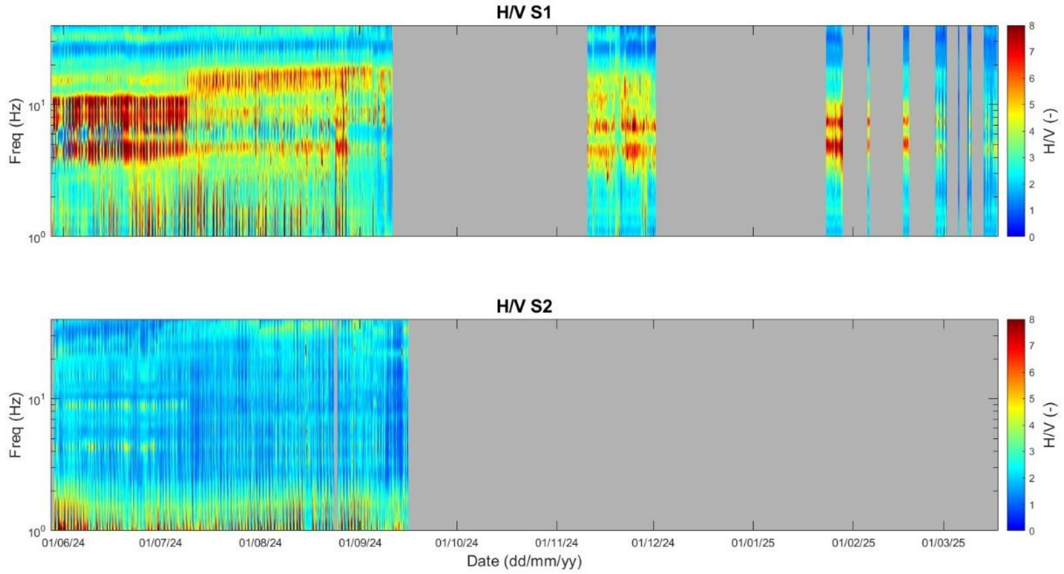

(b)

Figure 25: (a) H/V probabilistic distribution, data from 28 May 2024 to 18 March 2025. The black line is the mean value, black dashed lines are the 10th and 90th percentiles. (b)H/V over time for the two seismic stations in the period between 28 May 2024 and 18 March 2025. The grey areas are periods with no data.

Figure 25a shows the probabilistic distribution of the H/V spectral ratio for station S1. Two main resonance bands can be identified. The first one is between 4 and 5 Hz and corresponds to the frequency range highlighted by the first peaks observed in the horizontal PSD (Figure 23).

The second reference frequency is between 6 and 8 Hz, range that include the second peak of the horizontals PSD and the first peak detected in the vertical component.

For station S2, two weaker H/V peaks are observed again between 4 and 5 Hz and around 9 Hz. The lower H/V values recorded at this station are consistent with its location on the stable side of the fracture. The horizontal and vertical components are in fact both more stable, with lower

H/V ratios. Conversely, station S1, is characterized by stronger horizontal component than the vertical one, resulting higher H/V amplitudes, especially in the mid-frequency range.

As previously mentioned in the PSD analysis, a sudden change in spectral amplitude is registered after the 9 July 2024 (Figure 25(b)). This variation is better seen in the station S1, but even if weaker is well detectable also in station S2.

Since this behaviour is observed in both stations, an instrumental issue can be excluded. The causes may be related to an external factor affecting the entire system.

Another important observation is that the increase in H/V amplitude is not reflected in a change in the reference frequencies, that remains stable. Therefore, the cause of this variation cannot be attributed to a mechanical activation of the fracture. This is also confirmed by extensometer measurements, which didn't register any acceleration of fracture opening during the same period. In particular, the detrended displacement data shown in Figure 20 appears to be around zero.

Since the comparison with other years is not possible due to the limited data availability, which also cover only a small portion of the year, we cannot determine if a similar event recurs annually in the same period or also in other times, to potentially associate it to meteorological variations.

Consequently, one possible explanation is that this change may be related to meteorological forcings, such as snow melting and increasing temperature, which could alter the constrains acting on the fracture and thus its mechanical behaviour and movement. However, additional observations and a longer monitoring period are required to further investigate these hypothesis.

Other changes in the amplitude are observed at the end of August 2024 and end of January 2025, while station S2 was not working.

Azimuth angle

To characterize the dynamic behaviour of the unstable rock mass, it is crucial to analyse the azimuth of the seismic signal recorded by the geophone. While spectral amplitudes provide information on the energy of the vibrations, azimuthal analysis defines the dominant direction of motion in the horizontal plane.

Monitoring azimuthal variations allows to verify if the oscillation direction is consistent with the structural constraints of the rock mass, such as the orientation of the fracture and the gravitational forcing. Variations in this angle is a key indicator of the coupling between the unstable block and the stable side, providing essential insights into the stability and the potential failure mechanism of the site.

The azimuth angle has been computed using data recorded by station S1. In Figure 26 the y-axis has been limited to 80° to better show the behaviour of the data.

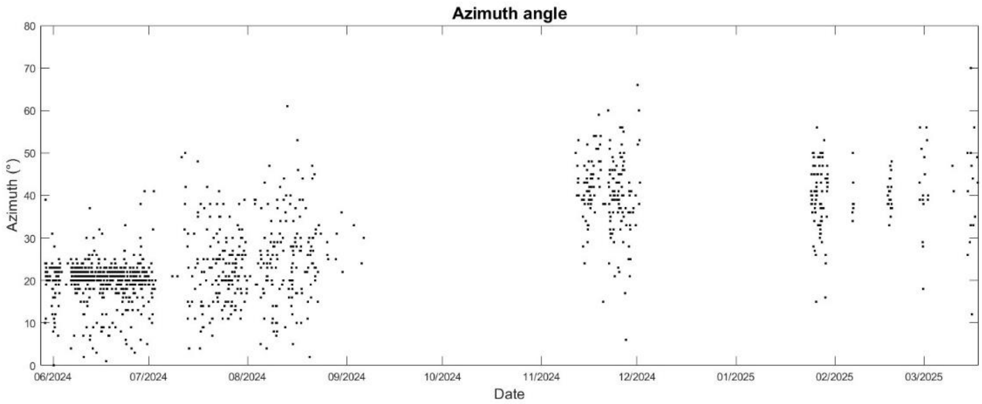

Figure 26: Azimuth angle distribution over time.

In the first part of the monitoring period (Figure 26), the azimuthal angle remains stable around 20°. Also in this case, a sudden change is observed around 9 July 2024, after which the azimuthal distribution seems more dispersed, indication of a greater variability in the main direction of oscillation of the unstable rock mass.

This variation may be due to changes in meteorological forcings that may have altered the mechanical constraints of the rock mass. Such modifications likely induced a shift in the oscillation direction, reflecting in a change in the structural response of the system.

Even if a lot of data are not available in the period after September 2024, the azimuth values appears to increase around 40° between November 2024 and March 2025, therefore a switch through the eastern direction has been observed.

The next chapter "Numerical model results" provides additional support for this interpretation. The azimuthal analysis suggests that after the 9 July 2024 the second vibration mode may become more significant with respect to the first mode, leading to a significant rotation of the azimuthal oscillation direction.

Figure 27 represents the occurrence frequency distribution of azimuthal angles based on 1219 observations. The maximum occurrence is observed at 21.5° from north, identifying the predominant direction of oscillation over the entire monitoring period.

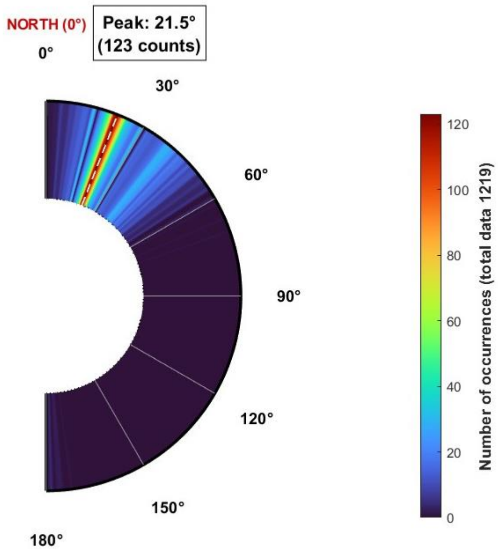

Figure 27: Occurrence frequency of the azimuthal angles. The white dashed line represents the angle with the peak of occurrences.

The relationship between the azimuthal variations and temperature was also investigated during the monitored period (Figure 28).

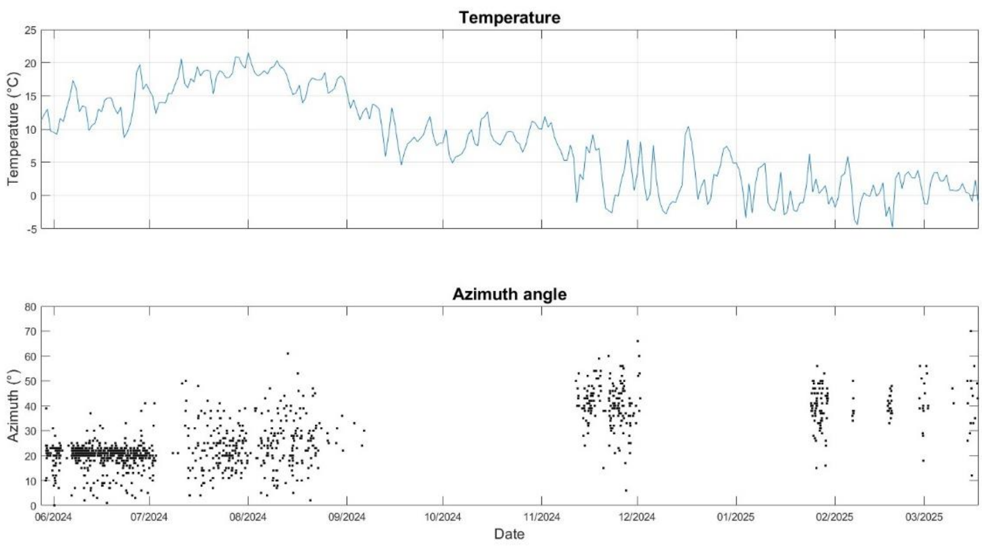

Figure 28: Temperature and azimuth angle confront.

An increase in the azimuth angle is generally observed with a decrease in temperature, whereas during the warmer period azimuth values appears lower. This behaviour may also be related to the thermo-mechanical response of the material, which could contract or expand as a consequence of temperature variations, thereby decreasing or increasing the mobility of the fracture.

As already discussed, it is difficult to make definitive statements because of several data gaps.

Temperature as driving mechanism at a daily scale

Due to the limited temporal extent of the available dataset, a long-term seasonal comparison is currently unfeasible.

However, at shorter timescales, the data reveal a clear daily cycle pattern. Consequently, this chapter focuses on evaluating the correlation between the observed seismic parameters and thermal forcings at a daily scale.

To achieve the necessary level of detail for this high-frequency analysis, hourly temperature records were used. This approach aims to isolate and identify the immediate mechanical response of the fracture to diurnal thermal expansion and contraction, providing crucial insights into how daily temperature gradients act as a primary driving mechanism of the oscillation patterns of the unstable rock mass.

In particular, the relation between temperature, H/V magnitude, and resonance frequency has been analysed. For this purpose, only the first resonance frequency from the horizontal to vertical spectral ratio (HVSR) has been extracted for both monitoring stations.

The first resonance frequency has been selected choosing the frequencies associated to the maximum peak of H/V within a selected range between 3 and 6 Hz.

The H/V magnitude was obtained extracting the value of H/V associated to each selected frequency. The results are shown in the first plot of Figure 29 and Figure 30. To better highlight the daily cycle, only one month of data is shown in Figure 29 and Figure 30. The month of June was selected because, in the period preceding 9 July 2024, the variation in H/V values are more clearly visible and pronounced.

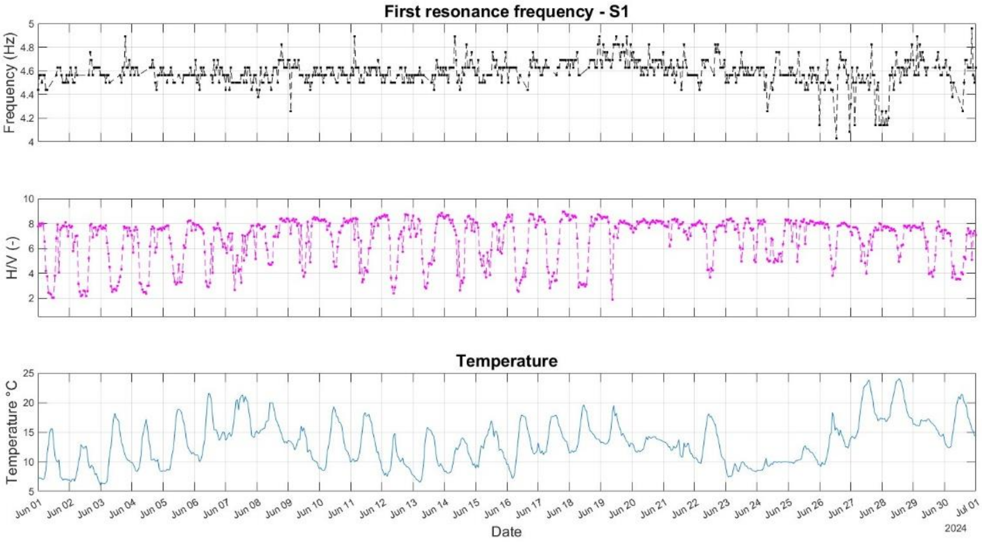

Figure 29: Temporal evolution of the first resonance frequency, H/V magnitude and temperature recorded at the station S1 in the period between 1 June 2024 and 1 July 2024.

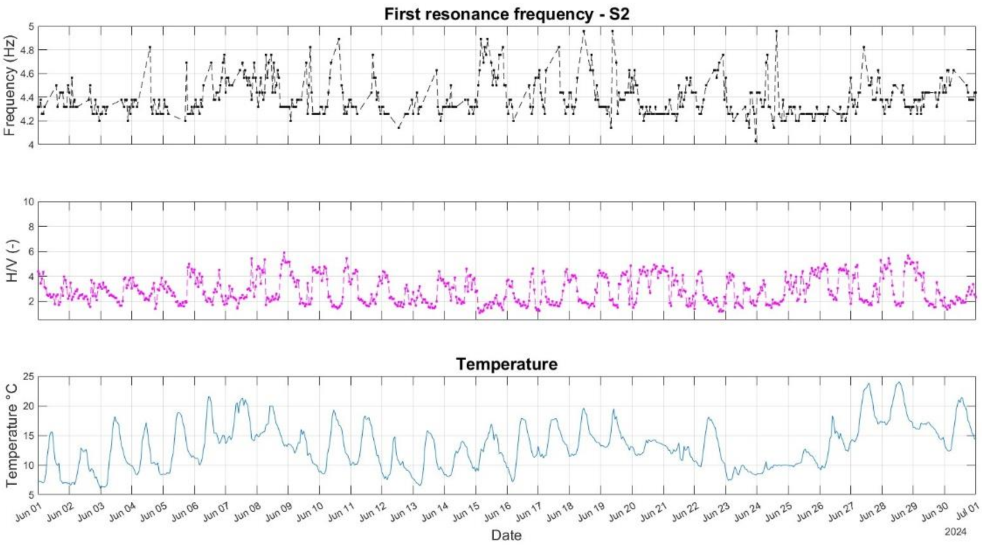

Figure 30: Temporal evolution of resonance frequency, H/V magnitude and temperature recorded at the station S2 in the period between 1 June 2024 and 1 July 2024.

It is possible to see that H/V magnitude seems to follow the daily temperature variations, while the frequency at S1 has very little variation around its mean value. For the frequency at S2, the observed variations appear larger. However, it is important to remember that the S2 spectrum was stable, therefore, these fluctuations can likely be attributed to the difficulty in accurately identifying the H/V peak within the resonance frequency range. Moreover, the H/V amplitudes for S2 still seem to follow a daily cycle, although they remain relatively low in magnitude.

To prove if a daily cycle is present in the data previously shown, a Fourier analysis has been carried out. Figure 31 reports of the spectrum for temperature. The main amplitude correspond to a frequency of 0,003 1/day, corresponding to a period of 333 days, therefore reflects the annual cycle. The second higher amplitude occurs at a frequency of 1/day, corresponding to the daily cycle as expected.

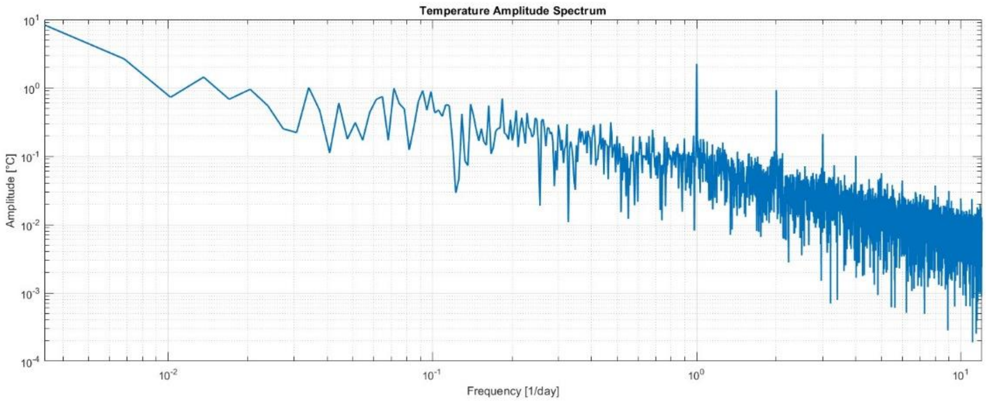

Figure 31: Amplitude spectrum resulting from Fourier analysis for temperature.

The same analysis has been done for the frequency and the H/V magnitude for both the stations, the corresponding amplitude spectra are shown in Figure 32 and Figure 33.

For all the Fourier analysis, the data of June 2024 has been considered.

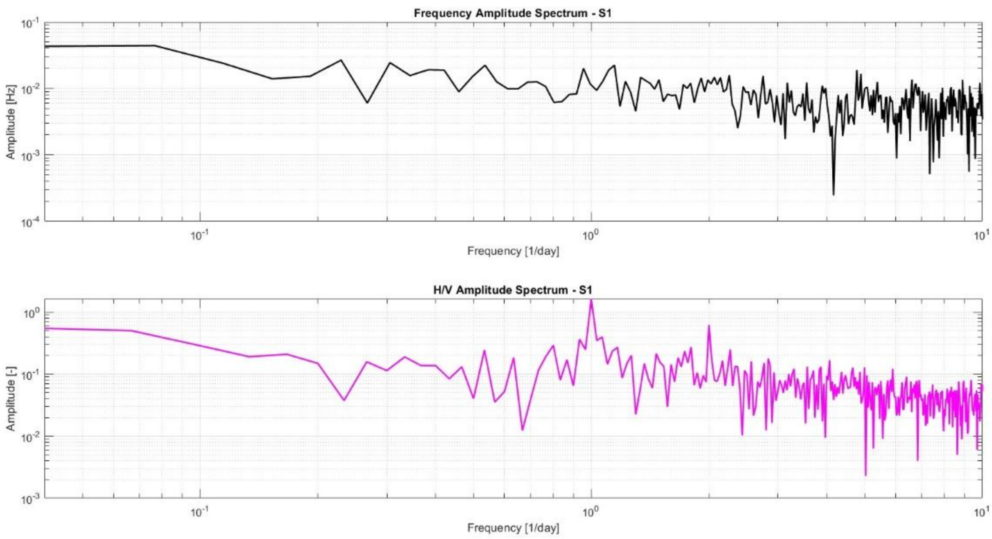

Figure 32: Amplitude spectrum resulting from Fourier analysis for frequency and H/V magnitude for the station S1.

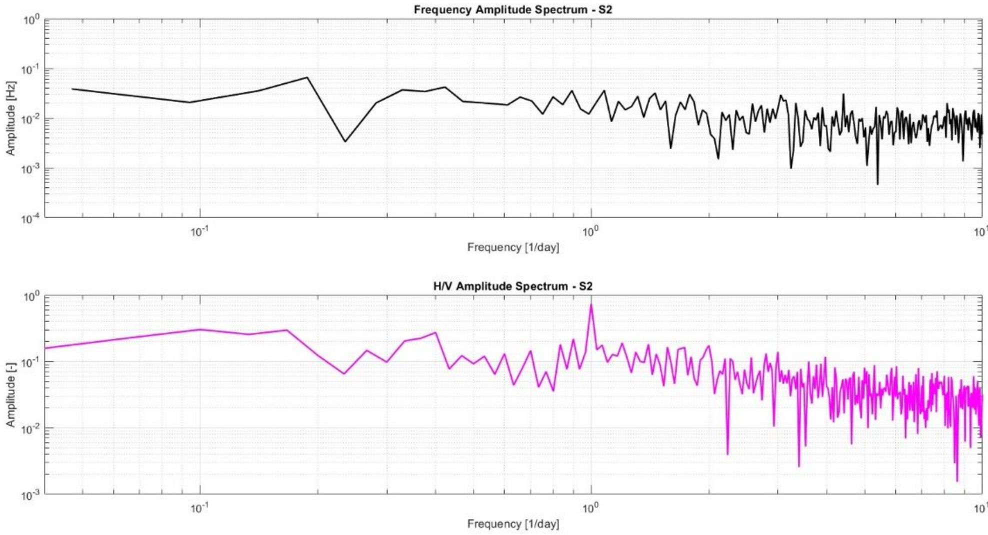

Figure 33: Amplitude spectrum resulting from Fourier analysis for frequency and H/V magnitude for the station S2.

The frequency amplitude spectrum appears complex, without a dominant peak and with no detectable daily periodicity.

Since resonance frequency variations mainly depend on variation of the fracture's structure, it is reasonable that a short-term variation of temperature, such as the daily cycle, cannot produce a sudden modification in the material and therefore in the resonance frequency. Instead, frequency can be affected by temperature driving mechanism at a seasonal scale, in this case in fact the variations of temperature are larger, and the material has the time to adapt and the deformation of the fracture to become more evident.

On the contrary, the relationship between H/V and temperature seems evident. The H/V amplitude spectra of both stations show a dominant peak corresponding to a period of one day, indicating that this is the primary contribution to the observed sinusoidal behaviour of the signal.

It is therefore interesting to understand how H/V magnitude changes with respect to the temperature cycle. To do so, only station S1 is being considered, being the one placed over the unstable rock mass and the one with higher variation of H/V magnitude over time.

Figure 34 presents a detailed view of the distribution of H/V magnitude and temperature records during the first week of June 2024 for station S1.

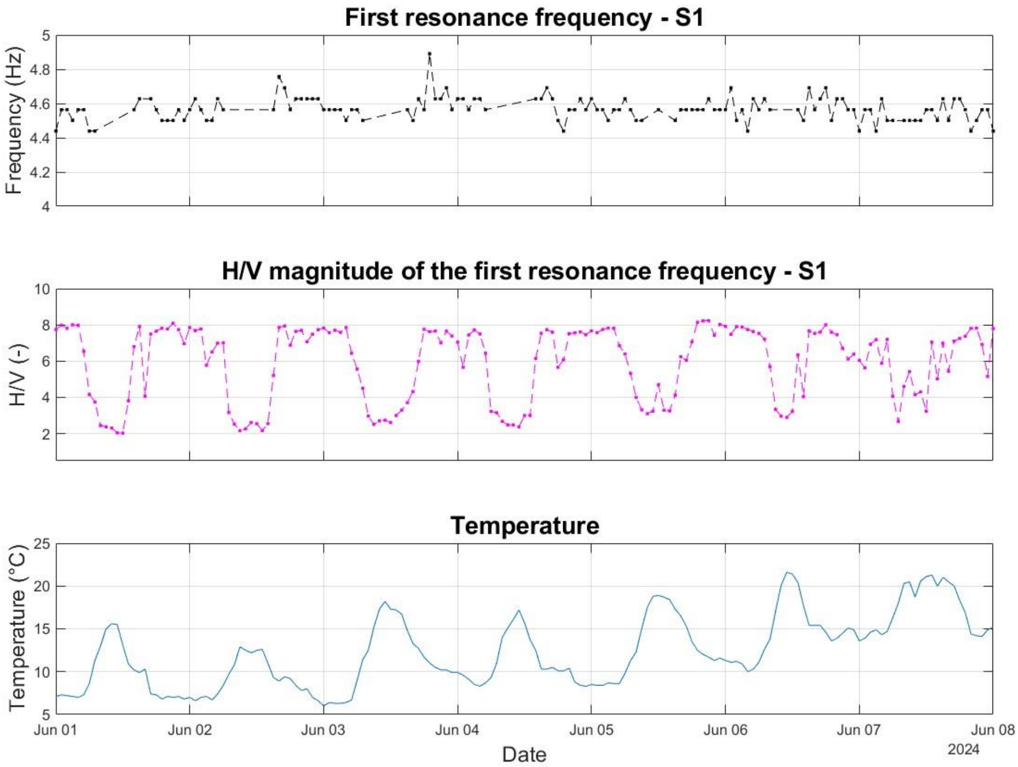

Figure 34: Resonance frequency, H/V magnitude of station S1 and temperature from 1 June 2024 to 8 June 2024

From Figure 34 an inverse relationship seems clear: whenever the temperature is increasing, the H/V magnitude is decreasing and vice versa.

This behaviour seems clear in the selected week, however, a more analytical approach was adopted to determine if this trend is observed throughout the entire month.

Therefore, from Fourier analysis a model of the mathematical wave describing H/V and temperature has been computed using the first 30 dominant spectral peaks. Those two curves have been than plotted together after their normalization (Figure 35).

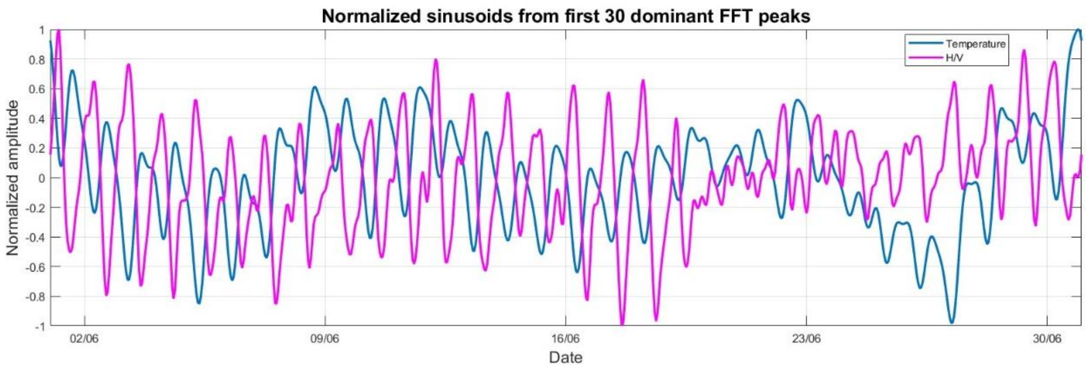

Figure 35: Normalized sinusoids corresponding to the first 30 peaks of frequency from the Fourier analysis for temperature and H/V magnitude.

Despite this simplification, it is still difficult to assess if the H/V magnitude is in phase with temperature. Therefore, a cross-correlation analysis between the two normalized sinusoids was performed.

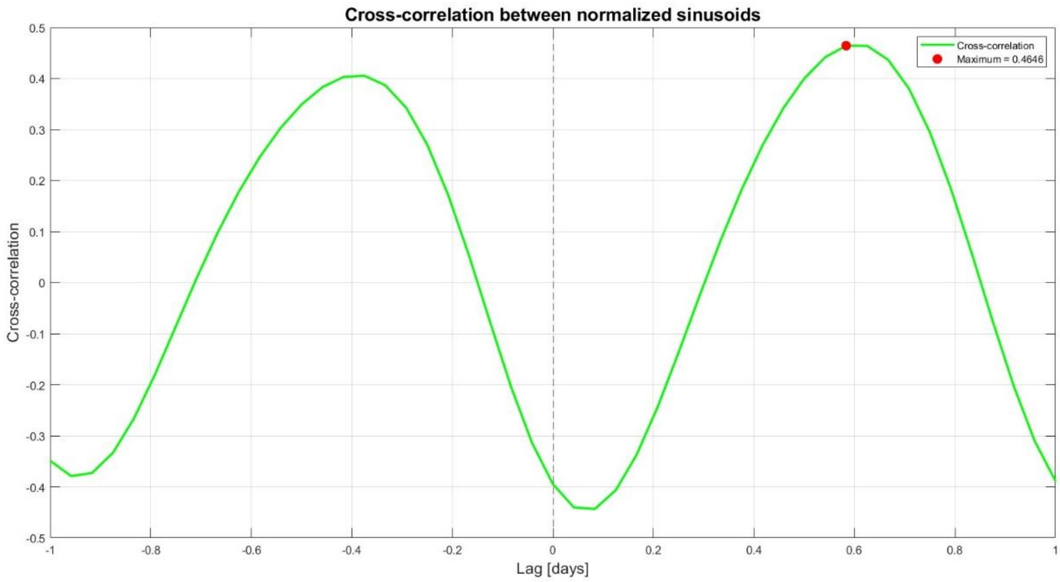

Figure 36: Cross-correlation between the normalized sinusoids of temperature and H/V magnitude.

Figure 36 reports a maximum correlation coefficient of approximately 0.46 at a positive lag of about 0.58 days. This suggests a moderate positive correlation, with the H/V response delayed by nearly 14 hours with respect to temperature variations. The delayed response may provide further evidence of the thermos-mechanical effects affecting the properties of the monitored rock mass.

The cross-correlation analysis was performed on the reconstructed harmonic signals obtained from the dominant Fourier components of temperature and H/V time series, rather than on the original raw data. Therefore, the resulting correlation does not represent the full variability of the system, which may also include transient effects, non-periodic fluctuations, and environmental noise.

The sinusoidal shape observed in the cross-correlation function is expected since periodic signals preserve their oscillatory nature during correlation analysis. As consequence, the cross-correlation function itself exhibits a quasi-sinusoidal behaviour.

In this case, the two positive peaks occurring at approximately −0.4 days and +0.6 days are separated by a time lag of about 1 day. For these lags, the cross-correlation is positive, which indicates a positive relationship between temperature and H/V.

It is also important to note that the cross-correlation function exhibit a negative peak observed at around 0.1 days (approximately 2.4 hours). This suggests an anti-phase relationship occurring about 12 hours before the main positive correlation peak.

Overall, the two statements are consistent with each other because cross-correlation can exhibit multiple peaks, each representing different temporal dependencies.

In conclusion, H/V magnitude shows a clear relationship with temperature, whereas the resonance frequency does not exhibit a daily cycle. A more robust analysis could be performed through the analysis of a longer dataset, which would also allow for the investigation of seasonal variability.

Furthermore, this analysis was performed using only one month of data. Although a longer dataset was available, focusing on June 2024 reduced the influence of long-term trends and seasonal variability, highlighting the short-term dynamics between temperature and H/V. Consequently, the results obtained should be considered representative of the selected period and cannot be directly extended to the full annual dataset without further analysis.

Microseismic analysis

The total number of detected events from ambient seismic noise recorded at station S1 (from 28 May 2024 to 18 March 2025) was 7085. However, it is important to note that the seismic station was not continuously operational during the entire monitoring period, resulting in several gaps in the recorded dataset.

A manual classification of the detected events was performed to identify the main classes of seismic signals occurring in the monitored site. Based on the classification scheme described by Helmstetter et al. (2010) and Colombero et al. (2021), three principal event classes have been identified.

The first class consist of rockfall events or slip along pre-existing fractures (Figure 37), which are typically characterized by duration of the order of tens of seconds, slow emerging signal and generally exhibit a broad frequency spectrum centred at low frequencies.

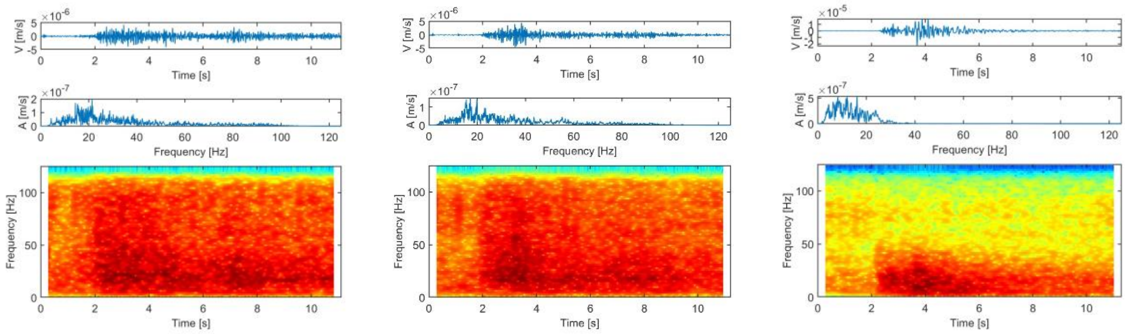

Figure 37: Results of the STA/LTA event detection method. Respectively referred to 04/06/2024 14:17:43, 04/06/2024 14:18:52 and 30/05/2024 17:53:23. The data format is: dd/mm/yyyy hh:mm:ss.

The second class of events are shorter in duration compared to rockfalls, typically few seconds, and generally are characterized by impulsive waveforms with almost triangular shape, with a clear high-frequency onset followed by an exponential decay. They may occur individually or as multiple events. This class may be associated with micro-cracking and micro-fracturing processes.

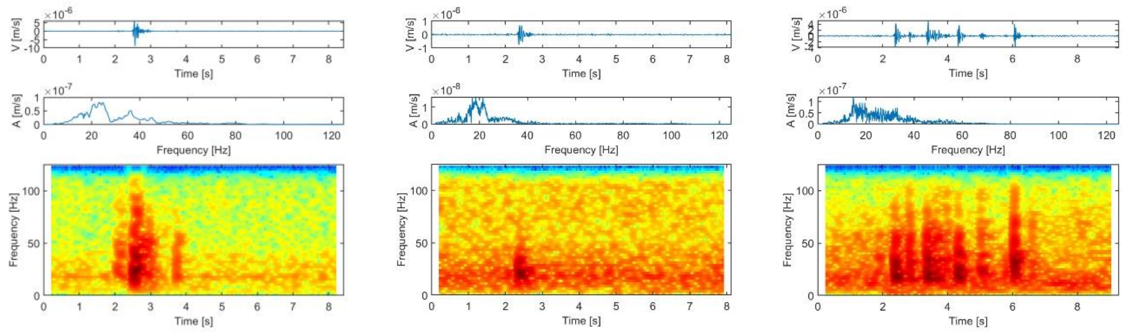

Figure 38: Results of the STA/LTA event detection method. Respectively referred to 13/07/2024 04:20:17, 09/07/2024 22:58:23 and 29/05/2024 13:33:37. The data format is: dd/mm/yyyy hh:mm:ss.

The third class of events includes short duration events. They have spectrograms with high amplitude vertical strips with frequency above 60 Hz. These characteristics may indicate that this class is associated with noise, in particular with rain drops (Figure 39).

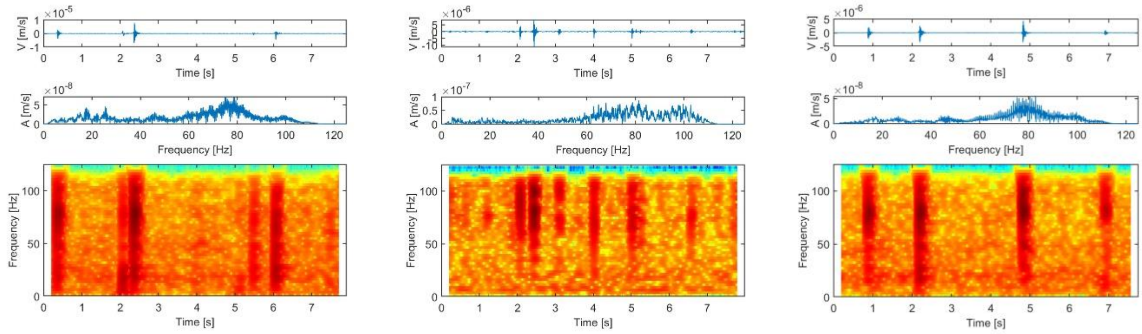

Figure 39: Results of the STA/LTA event detection method. Respectively referred to 22/08/2024 22:47:18, 12/06/2024 13:14:06 and 22/08/2024 22:46:39. The data format is: dd/mm/yyyy hh:mm:ss.

While machine-learning techniques could provide a systematic classification of the events, the primary aim of this study was the characterization of the overall microseismic activity of the monitored site rather than the development of an automated classification procedure. Therefore, the manual classification was adopted to identify the main classes of eventsand after that, the analysis focus on the statistical properties of the recorded seismicity.

Peak frequency of each event is computed as the frequency at which the maximum amplitude occurs in the signal amplitude spectrum. It is then plotted over time and compared to the cumulative number of detected events (Figure 40).

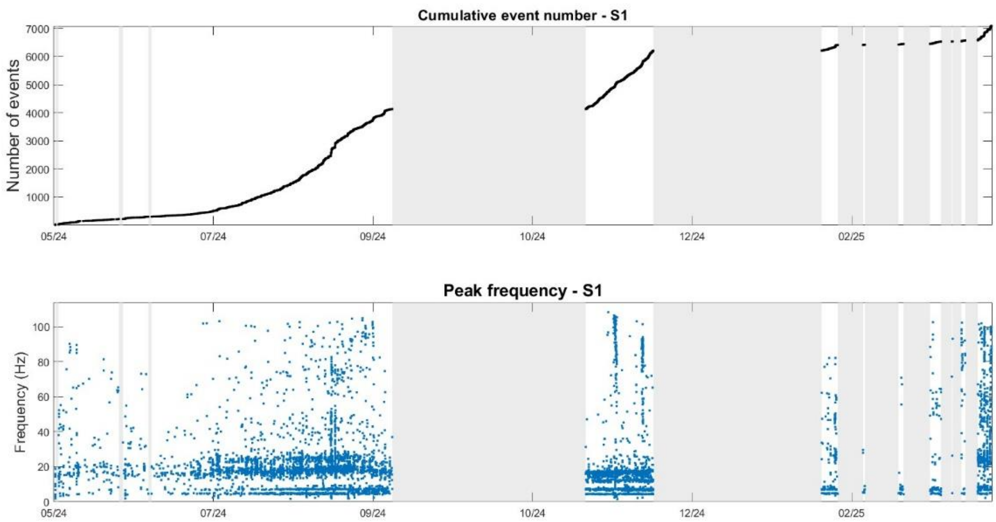

Figure 40: The first graph shows the cumulative events number, the second one the peak frequency distribution over time. The grey areas are periods without data.

The peak frequency distribution exhibit distinct horizontal bands, indicating the presence of preferred frequency ranges among the recorded events. The first dominant frequency is around 5 Hz and the second between 10 and 20 Hz. The recurrence of these frequency ranges suggests a certain degree of homogeneity in the mechanisms generating the recorded microseismic events.

A net change in the amount of event per day and their frequency distribution is visible after the 9 July 2024. This triggering point has also been observed in the azimuth angle graphs, in PSD and HVSR results. Figure 41 shows the comparison between the peak frequency variation over tome and HVSR.

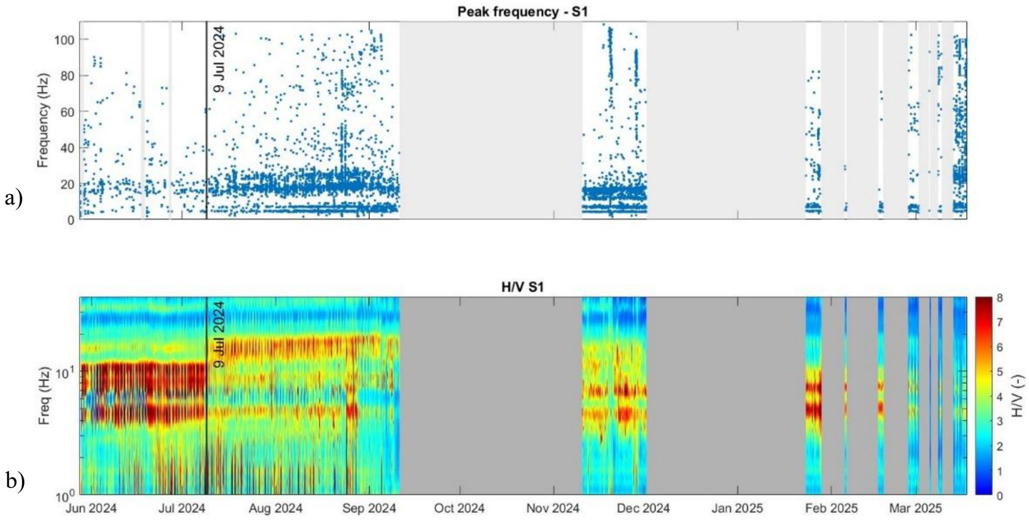

Figure 41: a) Peak frequency distribution over time of events recorded at station S1; b) HVSR over time for station S1. The grey areas are periods without data.

This change in the behaviour of both datasets supports the hypothesis of a modification in the mechanical constraints probably due to the material's response to temperature increases, as observed in the previous chapters. The higher freedom of movements after 9 July is reflected both in the wider dispersion of the azimuth angle data and in the increases number of microseismic events.

The comparison between the daily number of microseismic events and the extensometer measurements is particularly useful to investigate if the microseismic activity can be related to fracture opening (Figure 42).

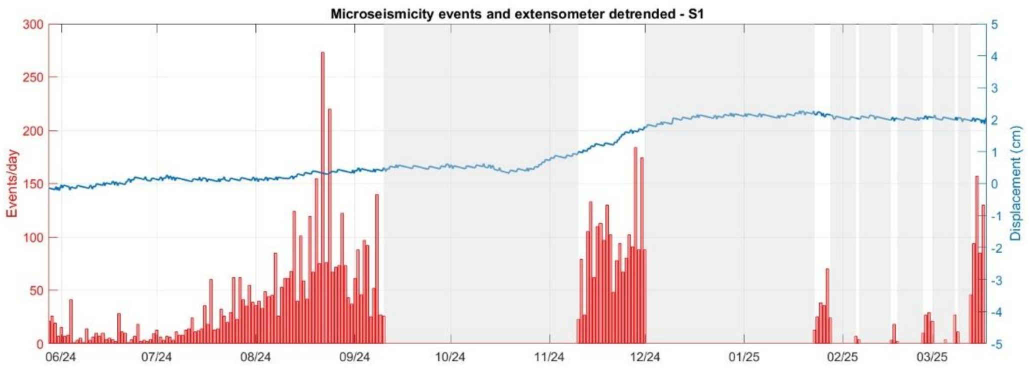

Figure 42: Extensometer detrended data over time (blue) and number of microseismic events per days (red).

From August 2024, the fracture exhibited an increase in the opening rate. This leads to the evident increase of the microseismic events that begin in the second half of July 2024.

The highest daily peak is reached on 22 August 2024, when 273 microseismic events were detected.

To assess if the meteorological factors may be the triggering factors for the occurrence of microseismic events, the daily number of events was compared with meteorological variables (Figure 43).

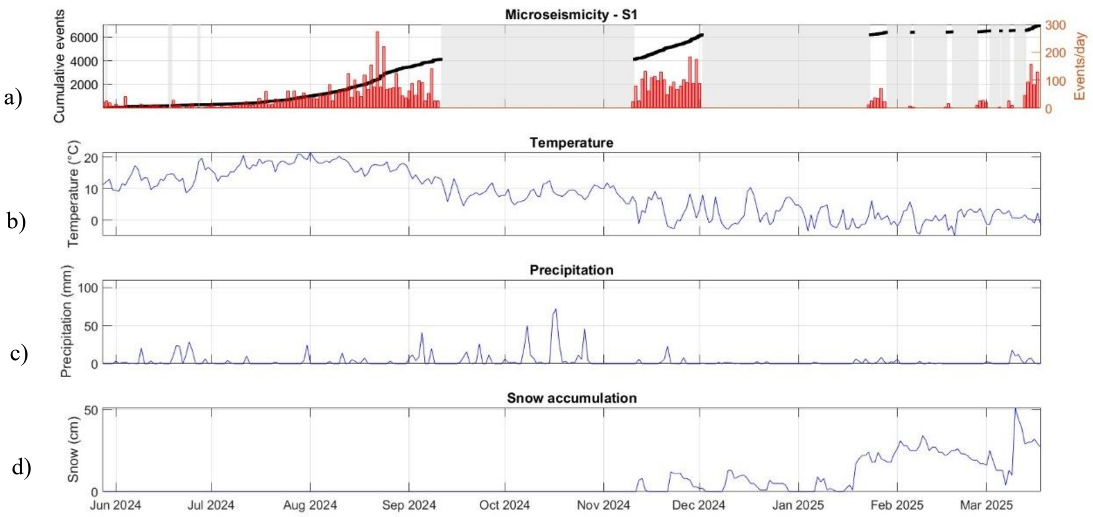

Figure 43: Comparison between daily number of microseismic events and meteorological variables. a) micorseismic events per day together with cumulative; b) daily temperature distribution; c) daily precipitation; d)snow accumulation.

The relationship between microseismic events and meteorological factors changes site to site. For example, the study of Helmstetter et al. (2010) at the Sechilienne rockslide highlighted a relationship between increased miscroseismic activity and precipitation events, together with a higher frequency of events in winter, under low temperature conditions. Instead, Levy et al.

(2011), studying the Vercors massif, observed a clear correlation with temperature variations, while no correlation with precipitation was found.

At the study site, no clear relationship can be identified with temperature or precipitations. The lack of data for sure limit the statistics and possibility to make assumptions.

To further investigate the temporal distribution of the detected microseismic events, the hourly occurrence histograms are computed (Figure 44). A comparison between the results from station S1 and S2 revealed a different occurrence of micorseismic activity. Indeed, they have a opposite behaviour: at station S1, MS events mostly occur during nighttime, while at S2 evets are concentrated during daytime hours.

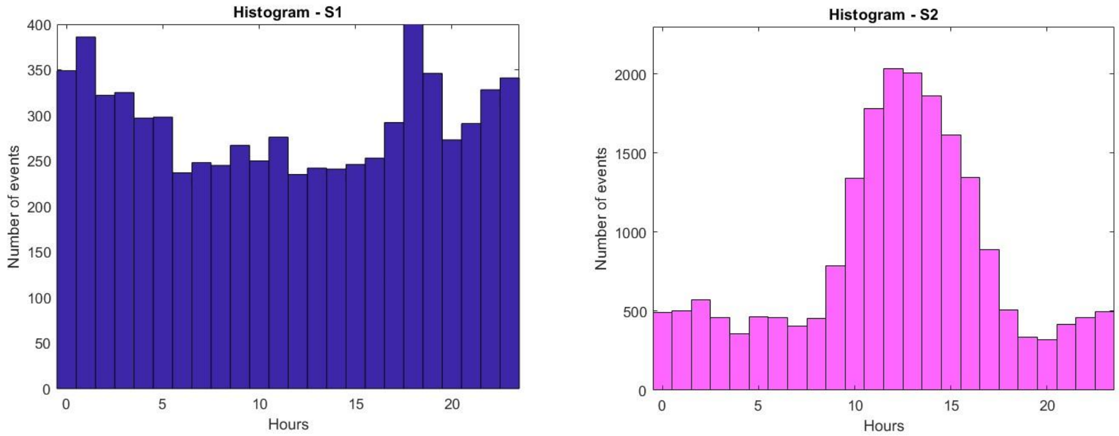

Figure 44: Hourly occurrence of MS events for S1 (blue) and S2 (magenta) for the period between 28 May 2024 to 18 March 2025..

The different daily probability of event occurrence is evident, despite the different total number of events recorded by the two stations.

The cumulative curves in Figure 45 highlight the different number of events detected by the two stations. This difference can be attributed to both the position of the stations and the characteristics of the STA/LTA event detection algorithm. In fact, the seismic station S2 exhibits a lower background noise, as evidenced by PSD analysis. Therefore, LTA magnitude is lower with respect to the one calculated in station S1. For the same STA values, this result in a higher STA/LTA ratio that consequently exceeds the imposed threshold.

Since STA/LTA parameters were the same for both the stations, station S2 is expected to detect a large number of events.

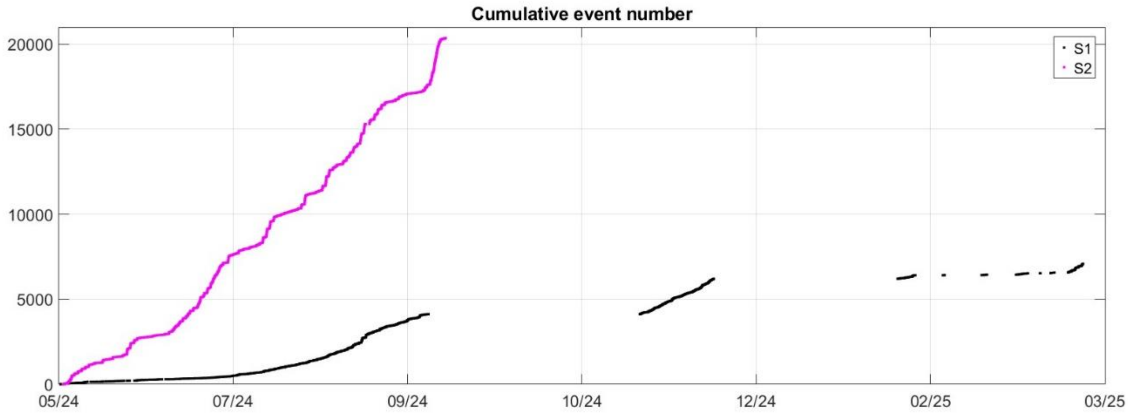

Figure 45: Cumulative event number curve for the two stations, S1(black) and S2 (magenta).

Since the recording activity of the seismic station S2 was interrupted on 15 September 2024, the subsequent analysis was limited to the period during which both the stations were recording.

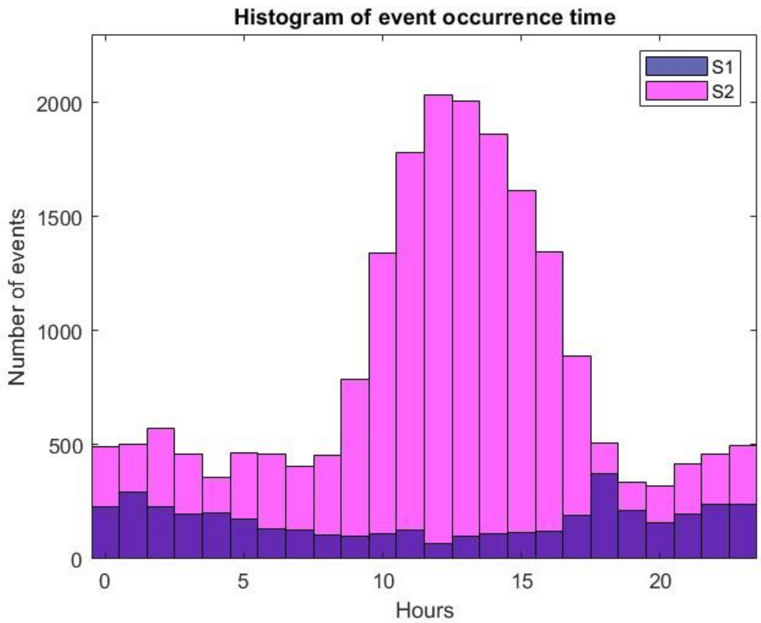

Figure 46: Histograms of hourly events occurrence for station S1 (blue) and S2 (magenta) from the 28 May 2024 to the 15 September 2024.

What can be inferred from this graph is that, in general, at S2 station more events per hour are detected with respect to S1. However, this difference becomes particularly pronounced during the central hours of the day, when the total number of events detected by station S2 exceeds that recorded by S1 by a factor of 15 to 30 over the considered period.

Therefore, a larger number of weak events are detected during daytime hours. Given the location of the seismic stations, an anthropogenic origin of this pattern appears unlikely. The causes should be researched among natural forcing mechanisms, such as temperature daily variation.

As previously observed for HVSR analysis, also microseismic activity in a quiet site can exhibits a daily cycle that appears to follow the temperature fluctuation.

Seismic stations analysis results for the second data collection (20th August 2025 – 17th March 2026)

The second dataset covers the period from 20 August 2025 to 17 March 2026. This dataset was retrieved during a field work carried out as part of the thesis, during which the seismic stations were inspected, maintained, and the recorded data were collected. It therefore represents the most recent monitoring period available for this study. Unfortunately, no data were recorded between the end of the first dataset, on 18 March 2025, and 20 August 2025. Similarly, no data were recorded between 17 March 2026 and the subsequent visit on 4 June 2026.

The second dataset was processed following the same methodology used for the first dataset.

The temporal evolution of PSD is shown in Figure 47 and the Horizontal-to-Vertical spectral ratio (H/V) is shown in Figure 48.

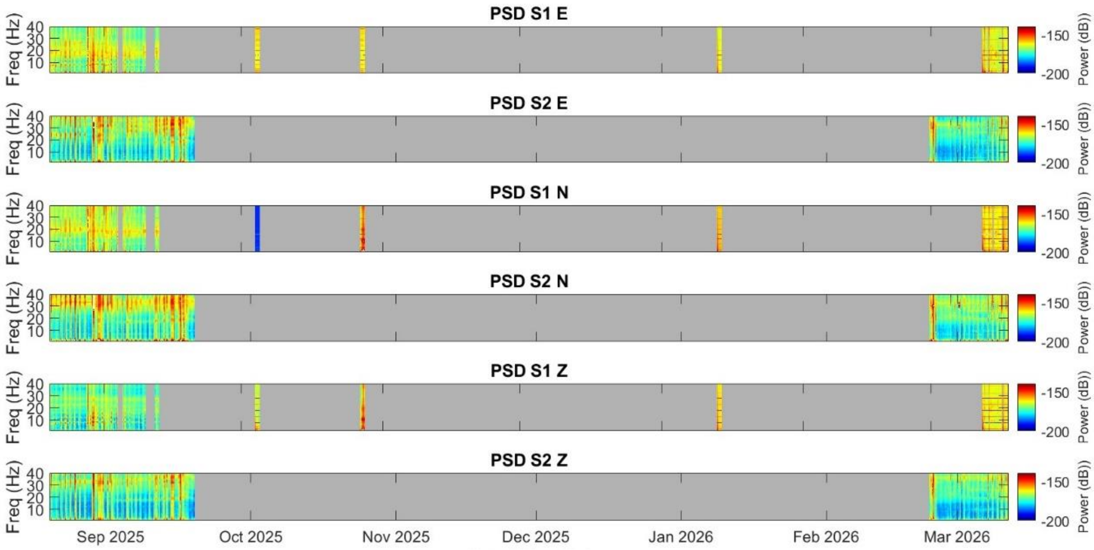

Figure 47: Temporal evolution of the PSD for the two seismic stations in the three components during the period between 20 August 2025 and 17 March 2026. PSD values are expressed in decibels (dB), computed as $10log10(PSD)$, where the reference value is 1 (m/s)²/Hz. Grey areas indicate periods with missing data.

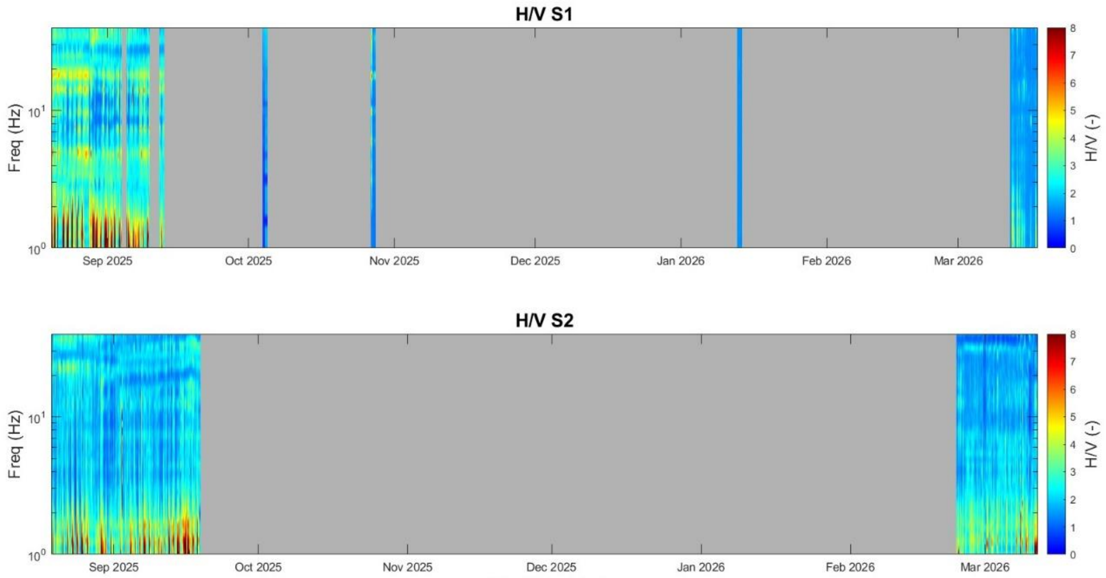

Figure 48: Temporal evolution of the H/V ratio for the two seismic stations in the period between 20 August 2025 and 17 March 2026. The grey areas are periods with no data.

As is evident, the available dataset is very limited and does not provide sufficient coverage to perform a seasonal cycle analysis or to allow a meaningful comparison with the data form the first dataset.

The lack of data is likely related to the stations' power supply system. Since the energy comes from the solar panels, the intense snow accumulation during the winter season may have reduced the power availability and consequently interrupted the data acquisition.

The installation of remote monitoring devices may be beneficial for checking the opreational status of the stations in real time and, where possible, restoring their functionality promptly.

Numerical model results

To complement the experimental observations and investigate the physical mechanisms controlling the observed dynamic behaviour of the system, a numerical model has been developed.

The main objective of the modelling approach was to reproduce, in a simplified but mechanically consistent way, the response of the system under different boundary conditions and geometrical configurations, allowing a direct comparison with the results obtained from the seismic data analysis.

The numerical model is based on a discretized representation of the investigated slope, where the geometry is idealized into a set of interacting blocks.

Particular attention has been given to preserving the characteristic dimensions and structural arrangement of the investigated site, so that the model can realistically represent the dominant deformation and vibration modes observed in the data. In this framework, the stable rock portion was represented by a block with dimensions of 250 m x 70 m in accordance with the geometrical reconstruction proposed by of A. Petroccia et al., 2020.

An additional stable block was introduced in front of the previous one and was used to extract and define the fracture void.

The unstable rock mass was then dimensioned to be consistent with the measurements obtained from QGIS analysis and information reported in the 2024 SiFraP survey, assessing a total volume of the unstable mass of about 15000 m^3. The final dimensions adopted in the model were 45 m x 65 m x 5.2 m.

The material properties (Young's modulus, density and Poisson's ratio) assigned to the model were derived from literature values and are reported in Table 2.

Table 2: Mechanical properties adopted in the numerical model.

Property	***Value***
Young's modulus	$15 \cdot 10^9\ Pa$
Density	$2650\ \frac{kg}{m^3}$
Poisson's ratio	0.25

With these constrains and by varying the fracture depth, the first four resonance frequencies were obtained through the numerical model. The final fracture geometry was of 45 m long, 0.5 m wide and 17.5 m deep.

The resulting first four resonance frequencies were 4.5796 Hz, 6.4175 Hz, 6.5544 Hz and 7.5842 Hz.

The results of the numerical model are consistent with the frequencies identified in the spectral analysis of seismic data. In particular, the first two resonance frequencies (Figure 49 and Figure 50, respectively) obtained from the model closely match those identified in the experimental data, supporting the reliability of the adopted geometrical and mechanical configuration.

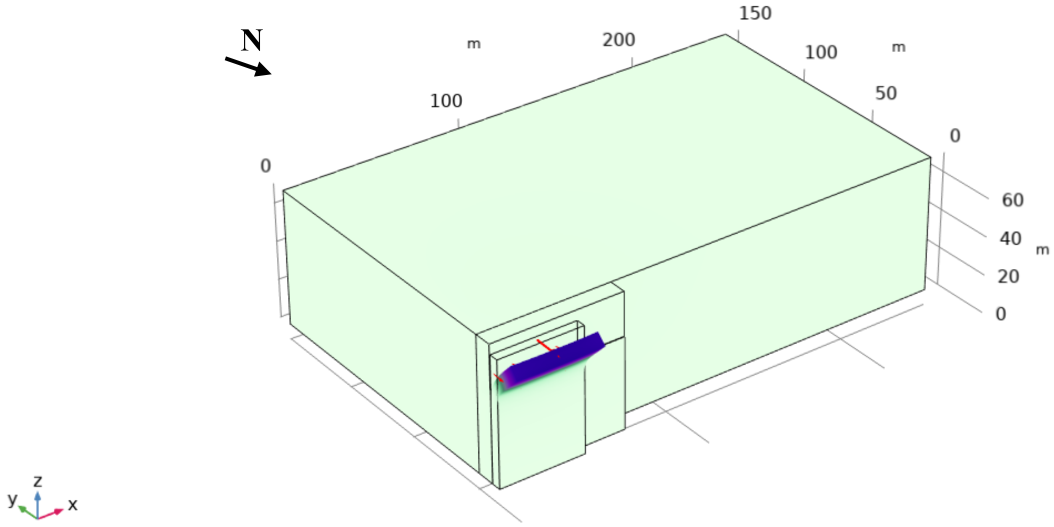

Figure 49: Representation by COMSOL Multiphysics of the first mode of vibration, referred to the resonance frequency equal to 4.5796 Hz.

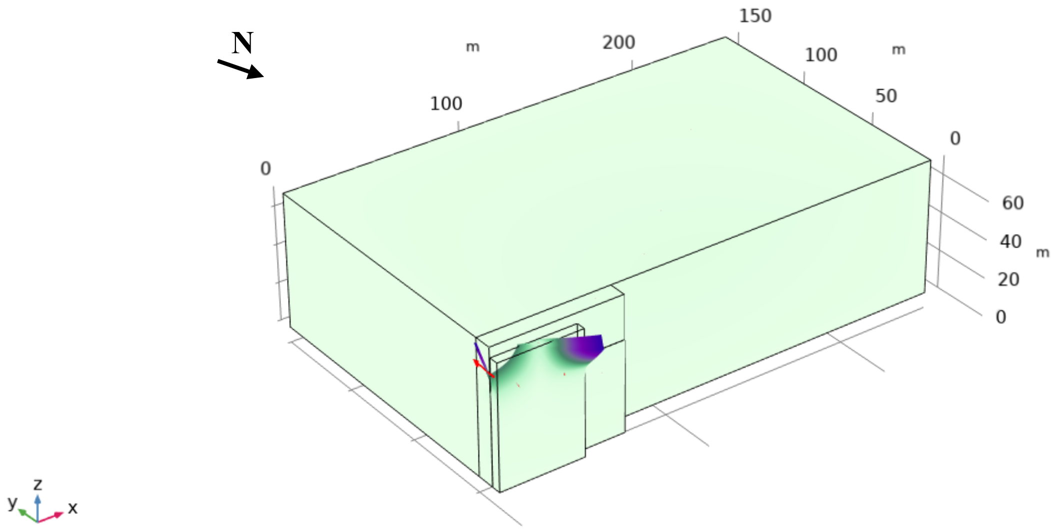

Figure 50: Representation by COMSOL Multiphysics of the second mode of vibration, referred to the resonance frequency equal to 6.4175 Hz.

Furthermore, the simulated vibration modes provide additional insight into the interpretation proposed in the previous chapter regarding the azimuth angle analysis. The seismic observations suggested that, during the first part of the monitoring period, the dynamic response of the unstable rock mass was mainly controlled by the first vibration mode. Subsequently, the contribution of the second mode appeared to become more significant. The numerical results seem to support this hypothesis, as the second vibration mode exhibits a direction of motion more parallel to the fracture surface. This behaviour is consistent with the evolution of the azimuth distributions identified in the seismic analysis.

This correspondence may indicate that meteorological factors, such as temperature variations, progressively modified the mechanical constraints acting along the fracture. As a consequence, the dynamic behaviour of the rock mass may have evolved toward conditions in which the second vibration mode became dominant and more clearly detectable in the seismic response.

Conclusions

This study investigated the influence of meteorological factors on the dynamic behaviour of the Gollone landslide through the integration of passive seismic monitoring, extensometer measurements, meteorological observations, and numerical modelling.

The analysis demonstrated that climate conditions play a significant role in controlling the behaviour of the unstable rock mass.

The investigation of the historical failures, occurred in 2011 and 2019, reports a connection with the intense precipitation events preceding the collapses. Moreover, both the events occurred in periods characterized by low, but still positive, temperature. These conditions are consistent with the mechanisms commonly reported in literature.

Extensometer data revealed the continuous opening of the monitored fracture, with accelerations phases associated with snowmelt periods. In this context, precipitation appears to have only a secondary role in driving fracture displacement, with the exception of particularly intense rainfall events, as the one occurred on the 17 October 2024, which preceded an acceleration of the extensometer displacement.

Passive seismic analysis identified two main resonance frequency bands, between 4-5 Hz and 6-8 Hz.

The HVSR analysis revealed a temporal variation in vibration amplitude, following a daily cycle. This variation has been found to be correlated with temperature daily cycle, showing an in-phase correlation with a delay of approximately 14 hours. These observations suggest that thermo-mechanical processes influence the dynamic response of the unstable rock mass.

On the contrary, the first resonance frequency seems to show a less defined daily cycle and a not clear correlation with temperature at daily scale.

The analysis of the azimuth angle highlighted a temporal change in the predominant vibration direction, suggesting a variation in the mechanical constrains of the fracture and a consequent change in the relative contribution of the different vibration mode.

Microseismic analysis provided further information on the activity of the landslide and contributed to the overall seismic characterization.

A sudden change in the fracture behaviour has been observed on 9 July 2024 through PSD, HVSR, azimuth angle and microseismicity analysis. This evidence indicates the occurrence of a probable modification of the fracture mechanical constraints at that time, resulting in changes in vibration energy, vibration direction, and the number of recorded microseismic events.

Numerical modelling successfully reproduced the first two observed resonance frequencies and through the simulation of the corresponding vibration modes supported the interpretation derived from the seismic observations.

Overall, the results confirm the strong interaction between climate-driven processes and rock slope instability. Among the meteorological factors investigated, temperature appears to have the strongest influence on the behaviour of the unstable rock mass.

Therefore, passive seismic monitoring is a valuable tool for detecting variations in the mechanical behaviour of fractured rock masses, and although the available dataset is limited in duration and affected by large data gaps, the study provides insights into the response of the unstable slope to environmental forcing.

Future works should focus on extending the monitoring period and improving the characterization of microseismic events throughout the use of machine learning.

Overall, this work represents the first step toward a complete characterization of the Gollone landslide. Long-term analysis, seasonal cycle investigations and comparison between years would, in future, provide a stronger statistical basis for the observed relationships and would allow to further validate the conclusion of this study.

Bibliography

Arpa Piemonte – Dipartimento Tematico Geologia e Dissesto; SiFraP; Scheda descrittiva di approfondimento – III livello; 2013.
https://webgis.arpa.piemonte.it/Web22/sifrap/iii_livelli/Gollone.pdf

Regione Piemonte Direzione Opere Pubbliche, Difesa del Suolo, Economia Montana e Foreste; 'EVENTO METEOIDROLOGICO del 4-8 Novembre 2011'; aggiornamento 21 novembre 2011. https://www.regione.piemonte.it/web/media/35062/download

SiFraP – Sistema Informativo Fenomeni Franosi in Piemonte; scheda riassuntiva delle informazioni contenute nel sistema informativo geologico di Arpa Piemonte per i dissesti di versante; 04-09-2024.
https://bdgm.arpa.piemonte.it/sifrap/sifrap_ii_liv_scheda.php?cod_frana=004-00678-00

Bottelin, P., C. Lévy, L. Baillet, D. Jongmans, and P. Guéguen. 'Modal and Thermal Analysis of Les Arches Unstable Rock Column (Vercors Massif, French Alps)'. Geophysical Journal International 194, no. 2 (2013): 849–58. https://doi.org/10.1093/gji/ggt046.

Bottelin, P., and L. Baillet. 'Original Insights Into Rock Slope Damage Processes Until Collapse From Passive Seismic Monitoring'. *Geophysical Research Letters* 51, no. 13 (2024): e2024GL109139. https://doi.org/10.1029/2024GL109139.

Brotóns, V., R. Tomás, S. Ivorra, and J. C. Alarcón. 'Temperature Influence on the Physical and Mechanical Properties of a Porous Rock: San Julian's Calcarenite'. Engineering Geology 167 (December 2013): 117–27. https://doi.org/10.1016/j.enggeo.2013.10.012.

Brune, James N., and Jack Oliver. 'The seismic noise of the earth's surface.' *Bulletin of the Seismological Society of America* 49.4 (1959): 349-353.

Burjánek, Jan, Valentin Gischig, Jeffrey R. Moore, and Donat Fäh. 'Ambient Vibration Characterization and Monitoring of a Rock Slope Close to Collapse'. Geophysical Journal International 212, no. 1 (2018): 297–310. https://doi.org/10.1093/gji/ggx424.

Colombero, C., L. Baillet, C. Comina, et al. 'Integration of Ambient Seismic Noise Monitoring, Displacement and Meteorological Measurements to Infer the Temperature-Controlled Long-Term Evolution of a Complex Prone-to-Fall Cliff'. Geophysical Journal International 213, no. 3 (2018): 1876–97. https://doi.org/10.1093/gji/ggy090.

Colombero, C., D. Jongmans, S. Fiolleau, J. Valentin, L. Baillet, and G. Bièvre. 'Seismic Noise Parameters as Indicators of Reversible Modifications in Slope Stability: A Review'. Surveys in Geophysics 42, no. 2 (2021): 339–75. https://doi.org/10.1007/s10712-021-09632-w.

Colombero, Chiara, Alberto Godio, and Denis Jongmans. 'Ambient Seismic Noise and Microseismicity Monitoring of a Prone-To-Fall Quartzite Tower (Ormea, NW Italy)'. *Remote Sensing* 13, no. 9 (2021): 1664. https://doi.org/10.3390/rs13091664.

Gariano, Stefano Luigi, and Fausto Guzzetti. 'Landslides in a Changing Climate'. Earth-Science Reviews 162 (November 2016): 227–52. https://doi.org/10.1016/j.earscirev.2016.08.011.

Häusler, M., C. Michel, J. Burjánek, and D. Fäh. 'Fracture Network Imaging on Rock Slope Instabilities Using Resonance Mode Analysis'. Geophysical Research Letters 46, no. 12 (2019): 6497–506. https://doi.org/10.1029/2019GL083201.

Helmstetter, Agnès, and Stéphane Garambois. 'Seismic Monitoring of Séchilienne Rockslide (French Alps): Analysis of Seismic Signals and Their Correlation with Rainfalls'. *Journal of Geophysical Research: Earth Surface* 115, no. F3 (2010): 2009JF001532. https://doi.org/10.1029/2009JF001532.

Lévy, C., L. Baillet, D. Jongmans, P. Mourot, and D. Hantz. 'Dynamic Response of the Chamousset Rock Column (Western Alps, France)'. Journal of Geophysical Research: Earth Surface 115, no. F4 (2010): 2009JF001606. https://doi.org/10.1029/2009JF001606.

Levy, Clara, Denis Jongmans, and Laurent Baillet. 'Analysis of Seismic Signals Recorded on a Prone-to-Fall Rock Column (Vercors Massif, French Alps): Analysis of Seismic Events Preceding a Rockfall'. *Geophysical Journal International* 186, no. 1 (2011): 296–310. https://doi.org/10.1111/j.1365-246X.2011.05046.x.

Ltd., G. S. (2019). Dm16-r8 / dm16-r16 digitizer: Man-d16-0001– chapter 4: Sta/lta triggering [Available online: https://www.guralp.com/documents/html/MAND16-0001/s4.html (accessed DATE)]. G¨uralp Systems Ltd. UK.

Maresca, Rosalba, Luigi Guerriero, Giuseppe Ruzza, Neri Mascellaro, Francesco Maria Guadagno, and Paola Revellino. 'Monitoring Ambient Vibrations in an Active Landslide: Insights into Seasonal Material Consolidation and Resonance Directivity'. *Journal of Applied Geophysics* 203 (August 2022): 104705. https://doi.org/10.1016/j.jappgeo.2022.104705.

Mirnezhad, M., M. Modarresi, R. Ansari, and M. R. Roknabadi. 'Effect of Temperature on Young's Modulus of Graphene'. Journal of Thermal Stresses 35, no. 10 (2012): 913–20. https://doi.org/10.1080/01495739.2012.720214.

Pachauri, R. K., Leo Mayer, and Intergovernmental Panel on Climate Change, eds. Climate Change 2014: Synthesis Report. Intergovernmental Panel on Climate Change, 2015.

Peterson, Jon R. '*Observations and modeling of seismic background noise'*. No. 93-322. US Geological Survey, 1993.

Petroccia, A., M. Bonasera, F. Caso, et al. 'Structural and Geomorphological Framework of the Upper Maira Valley (Western Alps, Italy): The Case Study of the Gollone Landslide'. Journal of Maps 16, no. 2 (2020): 534–42. https://doi.org/10.1080/17445647.2020.1784806.

Trnkoczy, Amadej. "Understanding and parameter setting of STA/LTA trigger algorithm." *New manual of seismological observatory practice 2 (NMSOP-2)*. Deutsches GeoForschungsZentrum GFZ, 2012. 1-20.